Ocean Engineering 336 (2025) 121762

Contents lists available at ScienceDirect

Ocean Engineering

journal homepage: www.elsevier.com/locate/oceaneng

Research paper

Tsunami-induced loads on coastal structures: Experimental investigation and prediction

Oliver Millar *, Li Ma, Ioannis Karmpadakis

Department of Civil and Environmental Engineering, Imperial College London, South Kensington Campus, SW7 2AZ, London, UK

ARTICLE INFO

Keywords:
Wave-structure interaction
Tsunami loading
Momentum-flux
Coastal engineering
Laboratory analysis
Numerical validation

ABSTRACT

Tsunami events can have devastating impacts on coastal communities. In order to minimise fatalities and destruction of critical infrastructure, recent design codes provide methods for estimation of tsunami forces. However, loads are heavily dependent upon incident wave properties, and interaction with the surrounding structural arrangement. This study presents the results of an experimental investigation into the effect of wave condition and structural arrangement on loading. A new experimental apparatus is developed to enable simultaneous measurement of local loads on individual structures, and global forces on arrangements at city block scale. Wave breaking behaviour is varied through changing initial inundation. These results enable insight into the progression of wave loading through structural arrangements. The accuracy of loading predictions from design codes and a new momentum-flux method is investigated. These are implemented using kinematics and free surface inputs from SWASH and OpenFOAM simulations. Their validity is assessed through comparison to the laboratory results. Design code estimates using a drag formulation and the momentum-flux model satisfactorily recreate experimental measurements when provided with appropriately modelled wave inputs from OpenFOAM. The momentum-flux approach, which requires no empirical inputs, is shown to be more robust, demonstrating its potential for estimation of tsunami loads on coastal infrastructure.

1. Introduction

Many coastal communities worldwide are exposed to potentially catastrophic tsunamis, including major cities across Asia such as Jakarta, Manila and Osaka. For example, the 2004 Indian Ocean Tsunami and the 2011 Tohoku Tsunami together claimed more than 240,000 lives and destroyed hundreds of communities (Synolakis and Bernard, 2006; Goto et al., 2021). Preparation for such events is challenging due to their rare and random nature. Between 2000 and 2024, only 371 tsunamis were recorded, of which approximately 10 % involved fatalities (NCEI, 2024). Earthquakes are the primary cause of major tsunamis and were responsible for both the 2004 and 2011 events. They can also act as an indirect trigger through generation of submarine landslides, as in the 2024 Noto Tsunami (Mulia et al., 2024). While certain regions experience higher seismic activity and hence greater risk of tsunamis, location and ocean geography play a significant role in their onshore effects. Local bathymetry can result in devastation in some communities, whereas nearby locations remain unaffected (St-Germain et al., 2014).

Existing infrastructure is generally unable to withstand severe inundation. Robertson and Chock (2013) identified that nearly 100 % of residential light-frame structures were destroyed in the Tohoku Tsunami. Coastal defences such as breakwaters and sea walls can provide some level of protection, but the spatial extent of tsunami events often exceeds the coverage of coastal protection (Inagaki et al., 2025). Accordingly, tsunami warnings typically trigger evacuations to higher ground. However, despite the establishment of an international warning system in the aftermath of the 2004 Indian Ocean Tsunami (Zhang et al., 2023), the first waves can arrive with little notice. During the Noto Tsunami, communities experienced inundation within 30 minutes of the earthquake (Inagaki et al., 2025). This can render full evacuation impracticable.

An alternative to evacuation is the construction of tsunami-resistant buildings, designed to withstand tsunami loads and exceed maximum water levels (Robertson and Chock, 2013). This is supported by recent design codes, including ASCE 7–22 (Robertson, 2024), and the Japanese MLIT 2570 (Macabuag et al., 2018). These standards provide methods to calculate tsunami-induced loading. However, the effects of the complex hydrodynamics that occur in realistic coastal city configurations are not typically included. This leads to uncertainty in their ability to accurately represent loading characteristics, which the present work aims to address.

* Corresponding author.
E-mail addresses: oliver.millar18@imperial.ac.uk (O. Millar), l.ma@imperial.ac.uk (L. Ma), i.karmpadakis@imperial.ac.uk (I. Karmpadakis).

https://doi.org/10.1016/j.oceaneng.2025.121762
Received 14 March 2025; Received in revised form 2 June 2025; Accepted 3 June 2025
Available online 14 June 2025

Specifically, the present study employs carefully designed experiments to investigate the effect of different types of tsunamis and structural arrangements on loading characteristics. Both the local loading on individual buildings, located throughout a model coastal city, and the global loading on neighbourhoods are investigated. Using these results, insights are provided into tsunami wave loading on groups of structures, in particular the temporal behaviour and magnitude of forces. Importantly, this new experimental dataset is used to examine the accuracy of design code predictions, and validate a recently-developed momentum-flux model for the prediction of tsunami loading on structures. In this process, numerical simulations using well-established models such as SWASH (Zijlema et al., 2011) and OpenFOAM (Weller et al., 1998) provide the necessary free-surface and kinematics inputs to the calculations.

The paper continues with a brief literature review on the topic in Section 2. Section 3 contains a description of the experimental apparatus and methodology. The experimental results are presented and discussed in Section 4. In Section 5, the experimental waves are recreated using numerical simulations, and these are used to assess the effectiveness of MLIT 2570, ASCE 7–22 and a momentum-flux numerical scheme in Section 5. Conclusions are provided in Section 6.

2. Background

2.1. Tsunami wave modelling

Rossetto et al. (2011) define tsunamis as long gravity waves. These are of small amplitude in the open ocean and reach hundreds of kilometres in wavelength. Due to differences in their generation mechanisms, each tsunami event is unique and there is no unifying wave theory that provides a generally-applicable description. Similar to wind waves, tsunami events slow down and increase in amplitude as they undergo shoaling (Rossetto et al., 2011). Close to the shoreline, the leading edge of a tsunami wave may disintegrate and form into long turbulent bores (Baldock et al., 2012). These ride on top of the main tsunami wave, and are comparatively minor in height (Madsen et al., 2008).

Solitary waves have formed the basis for many laboratory investigations into tsunamis. This class of wave contains a single wave crest, which retains its shape as it propagates. This distinguishes them from the continuous wave trains associated with wind and swell (Baldock et al., 2012). The surface profile of solitary waves is found through solution of the Korteweg de Vries equation (Miles, 1979). The resulting solitary wave profile, $\eta(x,t)$, is given by:

$$\eta(x,t) = H\,\mathrm{sech}^2\sqrt{\frac{3H}{4h^3}}(x-ct), \tag{1}$$

where H is crest height, h is water depth, c is wave celerity, x is horizontal location and t is time (Madsen et al., 2008). The wavelength is inversely proportional to the ratio H/h. Reductions in crest height and increases in water depth cause wavelength to rise.

Hammack and Segur (1974) conclude that a positive initial disturbance of the water surface will eventually result in the formation of a solitary wave. This is a common justification for the use of solitary waves in tsunami modelling. Goring (1978) develops an algorithm for solitary wave generation with a piston-type wavemaker, and applies this in an experimental analysis of solitary wave behaviour on slopes. This is extended by Synolakis (1987) with analytical solutions of solitary wave run-up on constant-gradient beaches. Tadepalli and Synolakis (1994)'s N-shaped waves were the first major departure from classical solitary wave theory (Synolakis and Bernard, 2006). N-waves better describe observations of shorelines receding before tsunami arrival, but are similar in wavelength to solitary waves.

Despite its historical use, Madsen et al. (2008) demonstrate that solitary waves contain significant shortcomings when used to model tsunamis. The propagation distances required for solitary wave formation, in line with the findings of Hammack and Segur (1974), are highly unrealistic on geophysical scales. In addition, the steepness of laboratory solitary waves are significantly greater than those observed in tsunami waves. Therefore, Madsen et al. (2008) recommend that studies consider wave profiles derived from field measurements or numerical simulations.

Recent studies have employed alternative methods of wave generation. Baldock et al. (2009) develop error function (ERF) waves for a piston-type wave paddle. By allowing the wavemaker to use its full movement range, greater control over the wavelength is achieved. Winter et al. (2020) define the paddle motion required for generation of ERF waves as

$$x_p(t) = \frac{S_{\max}}{2}\left(1+\mathrm{erf}(S_F(t-t_0))\right), \tag{2}$$

where the paddle position, x_p, is equal to zero until paddle motion begins, and $x_p = S_{\max}$ after it is complete. $S_{\max}$ is the paddle stroke length, S_F is a scaling factor, and t_0 is an initial time offset. The error function, erf is defined as

$$\mathrm{erf}(y) = \frac{2}{\sqrt{\pi}}\int_0^y e^{-t^2}\,\mathrm{d}t, \tag{3}$$

where y is the input to the function.

A separate set of investigations has focused on dam-break waves, including Yeh (2007), Santo and Robertson (2010), Nouri et al. (2010) and Palermo et al. (2012). In these studies, the rapid release of large volumes of water creates a turbulent hydraulic bore, similar to tsunami-induced bores. This waveform has been studied in detail by Chanson (2005), using video footage from the 2004 Indian Ocean Tsunami to demonstrate that it provides a reasonable representation of tsunami inundation.

Further studies have considered more complex wave profiles. Thusyanthan and Madabhushi (2008) and Heller et al. (2021) generate waves by dropping blocks into still water, while Lukkunaprasit et al. (2009) and Chinnarasri et al. (2011) apply a similar approach using an elevated tank of water. Prasetyo et al. (2013) and Tomiczek et al. (2016) combine constant flow pumps and piston-type paddles. Rossetto et al. (2011) show that a pump-based wavemaker is able to accurately recreate field measurements of the 2004 Indian Ocean tsunami. Finally, Goseberg et al. (2013) use a pump setup to precisely reproduce numerical results.

In this study, ERF waves are employed. These are the most appropriate waveform given the available wavemaking equipment, and improve control over scaling in comparison to solitary waves. While there are differences to the behaviour of realistic tsunamis, in particular with regards to scaling and the presence of wave breaking, ERF waves provide insight into the impact of the leading edge of the tsunami. This is arguably the most important part of the wave profile in terms of the applied loading, as it represents the first point of contact between the incident wave and the structure. As such, ERF waves are regularly used in similar analyses (see for example Park et al., 2019, Winter et al., 2020, Moris et al., 2021, and Zhang et al., 2023).

2.2. Tsunami load modelling

A number of empirical approaches exist for modelling the tsunami loads on individual structures. The Japanese tsunami design code, MLIT 2570, recommends that lateral fluid loading is applied as an equivalent hydrostatic force. The recommended approach for determining horizontal force (F) is,

$$F = Ba\rho gh, \tag{4}$$

where ρ is water density, g is gravitational acceleration, and B is the cross-flow width of the structure (Macabuag et al., 2018). The water depth coefficient, a, is varied between 1.5 and 3 depending on distance from the shoreline and the presence of seaward obstacles (Fukuyama et al., 2012). This approach is supported by the work of McGovern (2016), who find that the loads exerted by N-waves on a vertical wall are dominated by the hydrostatic component when wave breaking does not occur.

Foster et al. (2017) incorporate both hydrostatic and drag components in a Froude-number dependent loading formulation for rectangular structures, validating their model against experimental measurements. This is similar in principle to the recommended approach in the American standard ASCE 7–22, which considers hydrostatic, hydrodynamic and impulsive components (Chock, 2016). The hydrodynamic load is given through a drag formulation,

$$F = \frac{1}{2}\rho_s C_d B(hu^2) I_{tsu}, \tag{5}$$

where ρ_s is fluid density adapted to include debris, C_d is an empirical drag coefficient, and u is the incident flow velocity (Chock, 2016; Robertson, 2024). The tsunami importance factor, I_{tsu}, increases depending on the risk category of the infrastructure. An alternative drag-type approach is provided by Fujima et al. (2009), who recommend a variable coefficient that increases with depth of inundation, and reduces with distance from the shoreline.

ASCE (2021) recommends that the impulsive force, the instantaneous load applied as the wave front meets the structure, is taken as 1.5 times the magnitude of the hydrodynamic load. Arnason et al. (2009) find that the initial impulsive load on vertical columns becomes less significant as bore height rises, due to lower steepness of the incident bores. This indicates that impulsive loading is primarily dependent on the steepness of the wavefront.

In coastal communities, the incident waves are heavily modified through their interaction with infrastructure. These effects have been studied experimentally using groups of structures, often referred to as macroscale roughness elements (MREs). Simamora et al. (2007) consider six symmetrical MRE arrangements, and demonstrate that seaward structures can cause inaccuracies when applying empirical equations for force estimation on individual structures. The presence of seaward obstacles can cause the forces on structures to reduce (shielding), or increase (channelling). The presence and significance of these is dependent upon the wave condition and form of structural arrangement, as shown by Tomiczek et al. (2016) in their study of 3 symmetric MRE configurations. They find that shielding can reduce maximum pressure by between 40 % and 70 % when waves break amid the MRE. These are in agreement with the findings of Thomas et al. (2015), if the shielded structures fall within a 16° arc from the centreline of the seaward obstacle. If this wake angle is exceeded, forces can increase by up to 40 % when compared to free-field flow. Through examination of the interaction between broken ERF waves and a 10-row array, Moris et al. (2021) find that the maximum wave loading reduces by around 75 % when four or more rows provide shelter. The same experimental setup is applied by Zhang et al. (2023), who show that the presence of a partial seawall can cause loading to rise on structures immediately adjacent to the end of the defence.

On a larger scale, Park et al. (2013) used a 1:50 model of Seaside, Oregon, finding that the MREs reduced inundation velocity by 40 %. Fukui et al. (2022) observed similar results in their study of Kainan, Wakayama in Japan. Such larger-scale studies have enabled greater understanding of the complex flows that form within coastal communities. However, these problems have not been comprehensively investigated, and uncertainty remains regarding the importance of element size and relative spacing within MRE arrays, under varying wave conditions.

2.3. LMA

As an alternative approach to the above methods, Lagrangian Momentum Absorption (LMA) is a good candidate for the prediction of tsunami loads. This was developed by Ma and Swan (2020b) for calculation of wave-in-deck loading. This represents an improvement based upon Graaf et al. (1995)'s momentum formulation where the applied loading is assumed to be equal to the momentum-flux of the fluid entering the structure. This is defined as $F(t) = \dot{m}u$, where F is the applied force, $\dot{m}$ the mass flow rate of water into the volume of the topside structure, and u the initial horizontal velocity on the free surface at the time of entry. For a simple rectangular box of width b, the applied load must consider momentum-flux through the front face (F_f) and the underside (F_b),

$$F_f(t) = \rho u^2(\eta - h_d)b, \tag{6}$$

$$F_b(t) = \int_{x_c}^{x_f} \rho w u b \,\mathrm{d}x, \tag{7}$$

where w is the vertical water particle velocity, η the surface elevation at the front face, h_d the minimum level of the front face of the topside, x_c the horizontal position of the crest within the topside, and x_f is where the free surface exits the topside. Within the present study only F_f is relevant as there is no water ingress through the underside of the structure. This original momentum-flux formulation proposed by Graaf et al. (1995) assumes that all momentum is instantaneously transferred to the structure upon arriving at its boundaries. This neglects the fact that for any structure that incorporates some level of porosity, the momentum will be progressively transferred at a much lower rate. As such this solution provides an overestimate of the applied force.

LMA improves upon this by allowing the progressive transfer of momentum and therefore providing a more accurate and realistic solution. The method was originally proposed for the calculation of wave-in-deck loading, but is theoretically suitable for any porous structure that allows a partial through-flow, which is similar to structures (or groups of structures) that exist in coastal communities. The time-marched analytical method adopts a Lagrangian frame of reference, and is capable of incorporating any incident wave form. Importantly, no empirical loading coefficients are required in applying the model. The operating principles are described briefly here. For complete details and the full implementation of the model, the reader is referred to Ma and Swan (2020b).

In LMA, an incident wave is time-marched through a structure. At each time instance (t_i), the section of the wave about to enter the structure is divided into a large number of (n_i) momentum parcels (MPs) at the front face of the structure (or group of structures). Each parcel (identified by an ID k) is then individually tracked in a Lagrangian fashion during their progression through the structure. Momentum dissipation for each MP is estimated depending on the structural components encountered. This scheme is divided into two modules, for momentum intake and dissipation, as illustrated in Fig. 1. The momentum of an MP J_k entering the structure at each time instance t_i is given as:

$$J_{i,k} = \left(\frac{\mathrm{d}J}{\mathrm{d}t}\right)_{i,k} \Delta t, \tag{8}$$

where Δt is the time-step. It is assumed that the rate of momentum entry remains steady across each time-step. For every time instance, t_i, the total force is then calculated by summing the rate of change of momentum over all MPs (n_i):

$$F(t_i) = \sum_{m=1}^{n_i} \frac{\Delta J_m}{\Delta t}. \tag{9}$$

To describe the structure and its porosity, Ma and Swan (2020b) represent an offshore platform deck using a combination of two-dimensional screens and three-dimensional sponges. These can also be used to model coastal communities or the MRE arrays adopted in the present study, which are essentially dense structural arrangements with permeable properties.

Benefitting from the fact that the loading is strictly linked to the rate of momentum transfer from the wave to the structure, the method is

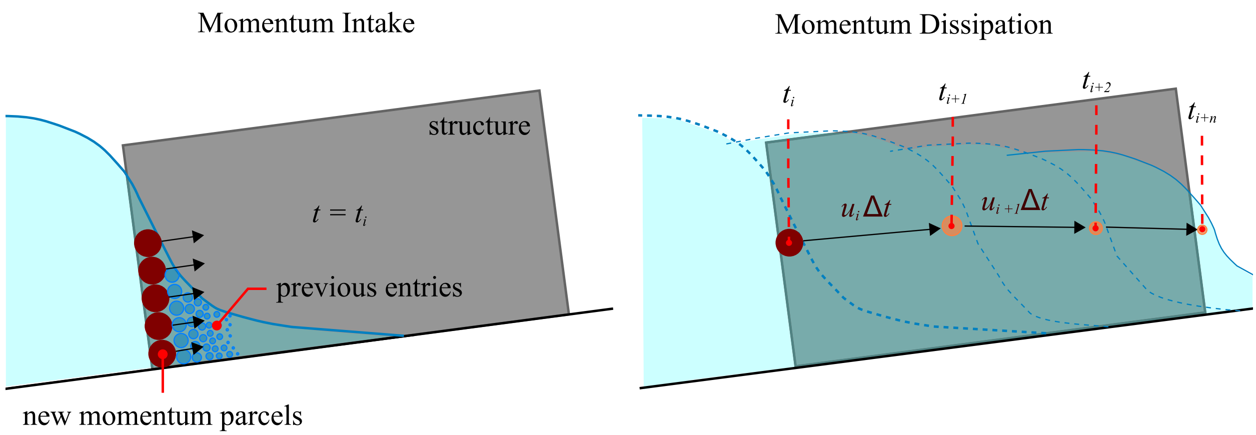

Fig. 1. Illustration of the two-step modelling procedure in LMA. The remaining momentum at each time step is indicated by the circle size. Adapted from Ma and Swan (2020b).

efficient and has been successfully applied to the prediction of wave-in-deck loading (Ma and Swan, 2020b, 2023). This was achieved under a wide range of different wave conditions, and has been shown to outperform existing models. As the only inputs necessary are surface profile and wave kinematics, LMA is in principle capable of accurate estimation of tsunami wave loading on MRE arrays. The key benefit of such a modelling approach is that it only requires the free-field flow characteristics. This applies both to tsunami-induced loading as discussed in the present paper, but also more broadly to other wave types. In applying LMA, each form of tsunami wave must only be modelled once. The resulting free surface and kinematics can be used to estimate loading on any structural arrangement, without the need to repeat the wave modelling. This is a major advantage when considering the design of new structures, or analysing different areas of existing infrastructure under the same wave conditions.

As a whole, this study presents the results of an experimental investigation into tsunami wave loading on large MRE arrays. This is achieved through a novel experimental apparatus, capable of simultaneously measuring the global loads on structural arrangements, and the forces on individual elements. The laboratory results are considered in combination with numerical simulations to assess the validity of load estimates from ASCE 7–22 and MLIT 2570, and investigate the potential of LMA for tsunami-load prediction.

3. Experimental study

3.1. Laboratory setup

Experiments were conducted within the coastal flume at Imperial College London (ICL). This is a glass-sided testing facility, 23 m long and 0.6 m in width. Waves were generated by a piston-type wavemaker, with automatic motion correction for active absorption of reflected waves. This is performed in the force domain, as discussed by Aknin and Spinneken (2017). Verification of the wavemaking capabilities of this facility can be found in past works involving direct comparisons to field data (Karmpadakis et al., 2020; Karmpadakis and Swan, 2022; Karmpadakis et al., 2022), extreme wave events (Huo et al., 2023) and operation of marine renewables Almalki et al. (2025). A uniform bed of stiffened PVC panels was installed at a slope of 1:15, starting 7.5 m from the wavemaker as shown in Fig. 2.

Surface elevations were measured using a high density array of 40 resistive-type wave gauges with a sampling frequency $f_s = 128$ Hz. The gauges were spaced at 500 mm intervals before the slope, and 200 mm intervals above it. The wave gauges were calibrated daily to ensure an accuracy of ± 0.5 mm, which has been extensively validated in previous studies such as (Karmpadakis et al., 2019; Karmpadakis and Swan, 2020).

After the wave is generated by the paddle (see Section 3.2), it propagates 15.35 m and loads the MRE array, where both the global loading on the entire array and local loads on individual elements are measured. Details of the arrays and loading measurement apparatus are provided in Section 3.4.

3.2. Wave generation

ERF waves were generated using Eq. (2). To allow rearrangement, the paddle stroke period, T, is introduced. This represents the time required for the paddle to complete its motion. Due to the properties of the error function, the paddle position x_p in Eq. (2) converges upon but never mathematically reaches the initial and final locations. Accordingly, an additional property ϵ must be defined. This is the acceptable offset from the front and rear limits of the paddle. The paddle position, x_p, is set to ϵ at $t = t_0 - \frac{T}{2}$, and $S_{\max} - \epsilon$ at $t = t_0 + \frac{T}{2}$. This allows solution for the scaling factor as

$$S_F = \frac{2}{T}\mathrm{erf}^{-1}\left(1 - \frac{2\epsilon}{S_{\max}}\right), \tag{10}$$

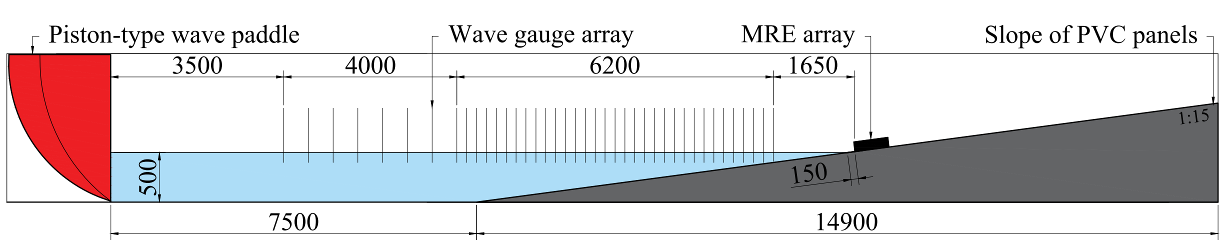

Fig. 2. Schematic of laboratory setup, including the position of the MRE (macro-roughness element) array.

Table 1
Wave case characteristics.

Label	Category	H (cm)	h (m)	T (s)
A1	Broken	5	0.5	7.05
A2	Broken	10	0.5	3.63
A3	Broken	15	0.5	2.26
B1	Breaking	6	0.55	6.49
B2	Breaking	8	0.55	4.95
B3	Breaking	15	0.55	2.25
C1	Unbroken	5	0.6	7.52
C2	Unbroken	10	0.6	3.95
C3	Unbroken	15	0.6	2.15

and through substitution into Eq. (2), x_p can be written solely in terms of ϵ, $S_{\max}$ and T. In this study, ϵ was set to 10^{-5}m throughout.

In order to generate the ERF waves, the wave surface elevation is required as an input to the piston-type wavemaker. As such, a relationship between η and x_p must be determined. Considering Goring (1978)'s method for generation of solitary waves, η and x_p are related through mass continuity at the face of the paddle,

$$\frac{dx_p(t)}{dt} = \frac{\eta\sqrt{gh}}{\eta + h}, \tag{11}$$

where $dx_p(t)/dt$ is the first derivative of the paddle motion with respect to time. Rearranging for η,

$$\eta = \frac{h\frac{dx_p(t)}{dt}}{\sqrt{gd} - \frac{dx_p(t)}{dt}}. \tag{12}$$

this provides a system of equations for the generation of ERF waves. The maximum stroke length, $S_{\max}$, was set constant at 0.48 m. Eqs. (2), (10), and (12) were solved iteratively by varying T until the maximum surface elevation was within 0.01 % of the target amplitude. A 256-second wavemaker cycle was selected. In this, the wavemaker gradually withdraws from the central position to its rearmost limits. It then moves forwards at $t = t_0 - \frac{T}{2}$, crossing the neutral axis at $t = t_0$, and reaching the forward limit at $t = t_0 + \frac{T}{2}$. After this, it slowly recedes to the central position. This cycle was selected to minimise disturbance and contamination of the ERF wave. The experimental wave heights were iterated to within 2 % of the theoretical values.

An example of the paddle motion and resulting wave behaviour is shown in Fig. 3. Fluctuations in the wavemaker motion after generation of the primary wave are caused by absorption of reflected waves from the slope. These, however, do not affect the loading data, as they occur after the main wave event. In addition, the experimental ERF wavelength was shorter than the theoretical value, as shown in Fig. 3 (b). This was consistent across all wave cases. It is partially caused by reductions in stroke period carried out during the amplitude iterations. It also indicates that the maximum stroke length of the wavemaker is slightly shorter than its nominal value. These differences were not investigated further, as full recreation of the theoretical behaviour is not required in this study.

3.3. Wave cases

The test matrix of incident wave cases was designed to allow investigation of the importance of wave amplitude, and the location of wave breaking. These are divided into three categories; waves breaking before (*broken waves*), amid (*breaking waves*) and after the loading rig (*unbroken waves*). The different breaking characteristics were achieved by varying the water depth between 500 mm and 600 mm. Three wave cases were chosen within each category, of small, medium and large amplitudes. The wave characteristics are given in Table 1. The wave amplitudes

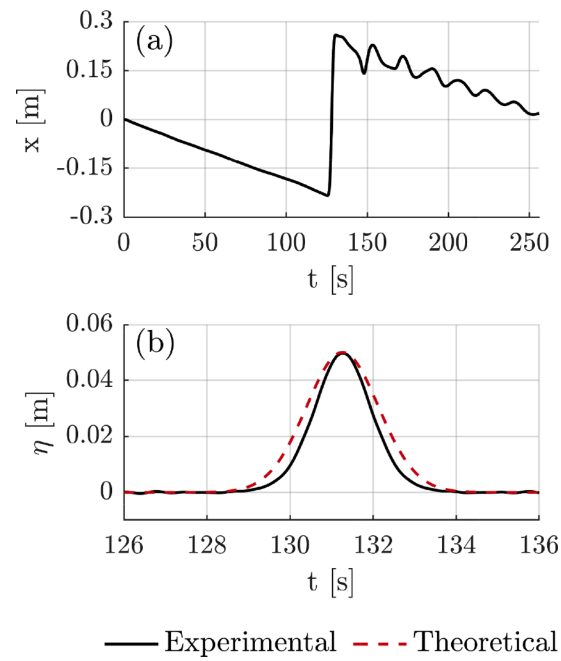

Fig. 3. a) Example of ERF paddle motion b) ERF wave as measured at the first wave gauge alongside a theoretical profile.

were selected at the toe of the slope, adopting a 1:100 length ratio between model and prototype scales. Froude number similarity was maintained between the two scales for all test cases. Scaling factors for the key quantities are provided in Appendix A.

Three repetitions were undertaken on each wave case to ensure high repeatability of the data. In addition, this enables ensemble averaging to accommodate the random turbulent behaviour that occurs after breaking.

3.4. Loading setup

The experiments investigated the global in-line loads on arrays of MREs, and the loads on individual structures within the arrays. The global loading rig is displayed in Fig. 4. A shear plate, which connects to the MREs on its upper surface, is 50 cm in width and 70 cm in length. The underside of the shear plate sits upon the supporting blocks at the up- and down-slope ends. The blocks, in turn, are connected to slider bearings on the lower plate, allowing the shear plate to move frictionlessly along the line of the slope relative to the lower plate. The lower plate is rigidly supported from the base of the flume and by the surrounding slope panels.

In order to measure the global loads on the MRE arrays, the supporting blocks are each restrained by two load cells on their outer faces. These are the only points of connection between the shear plate and fixed lower plate. They restrain the movement of the shear plate, and represent the only load path for in-line forces. This ensures that all relevant loads applied on the MRE array are transferred to the load cells.

In addition to the global loading measurement system, a hollow block was constructed for each array, as shown in Fig. 5, allowing measurement of the forces on individual MREs. These follow the same principles as the global loading rig. The blocks sit upon internal slider bearings, and are restrained by load cells on the inside of the up- and downstream faces. The individual loading blocks were moved throughout the rows of each array to assess the relationship between force and position, and provide validation for the global loads. The individual loading block was moved along the central column in arrays M6 and M10, and along the left-hand internal column in array M8.

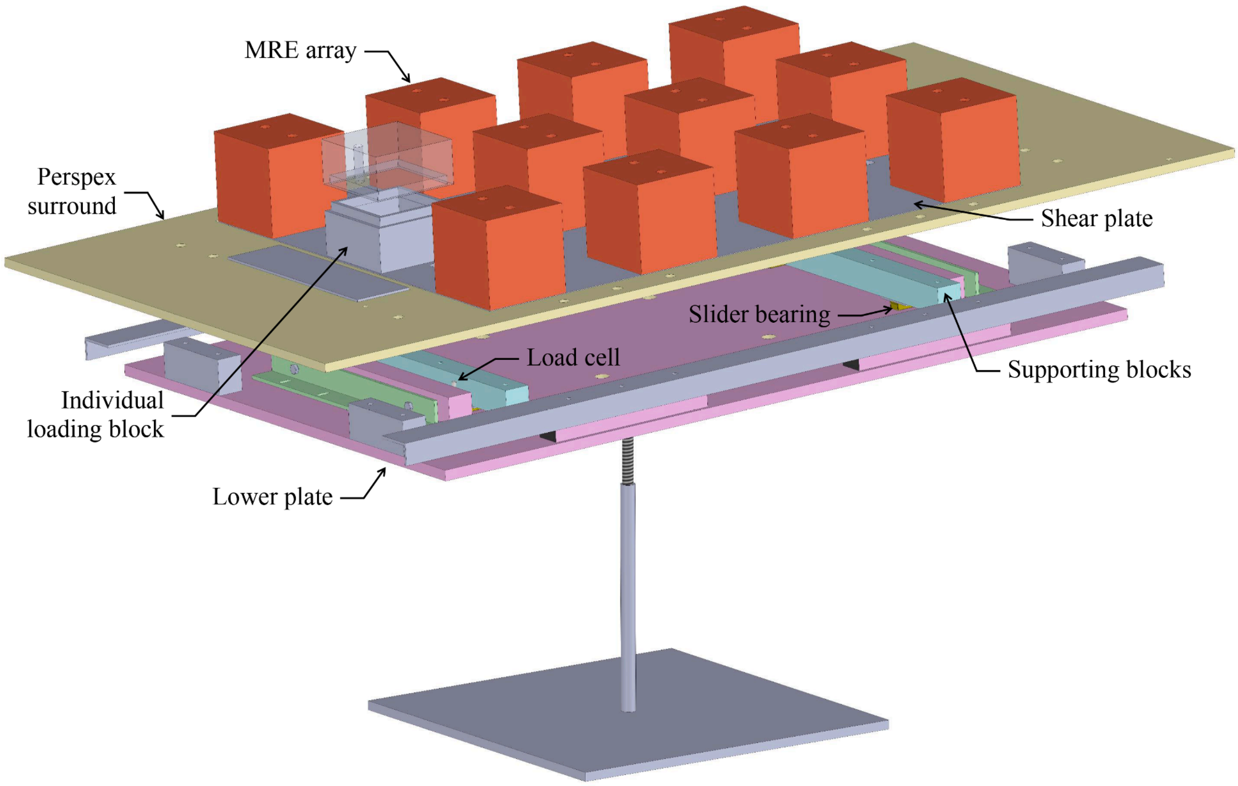

Fig. 4. Experimental loading apparatus with key components annotated.

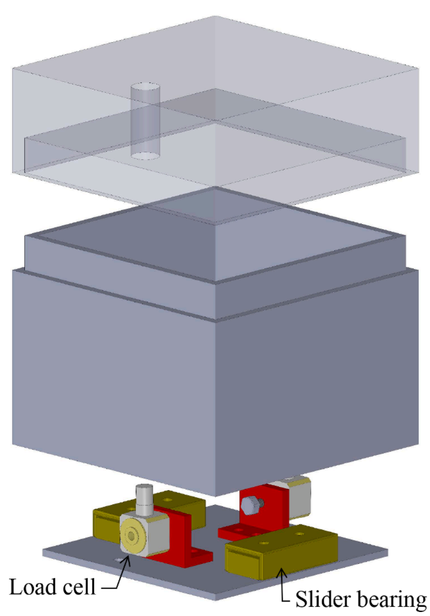

Fig. 5. M8 individual loading block.

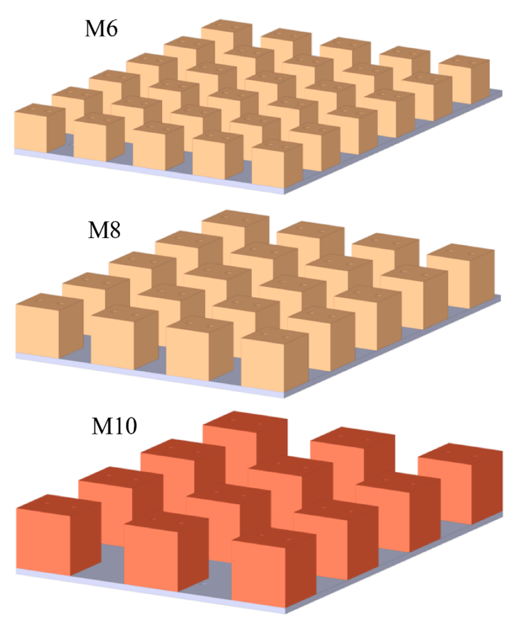

Fig. 6. 6, 8 and 10cm MRE arrangements.

Table 2
MRE Array characteristics, including number of rows (R), number of columns (C), block length (L), frontal area (A_f), plan area (A_p), and total volume (V).

Label	R	C	L (cm)	A_f (cm^2)	A_p (cm^2)	V (cm^3)
M10	4	3	10	300	1200	12000
M8	5	4	8	256	1280	10240
M6	6	5	6	180	1080	6480

A variety of structures can be attached to this versatile shear plate loading rig. In this investigation, systematically varying arrays of solid cubes were examined. Three grids with 6, 8 and 10 cm blocks were used; their arrangements shown in Fig. 6. These MRE arrays are designed to be generic representations of coastal communities, to ensure wide applicability of the results. The block positions were selected to allow formation of different flow patterns, with further details provided in Table 2. As shown in this table, the frontal solid area (A_f) and total solid volume (V) increase with element size. However, the plan solid area (A_p) is

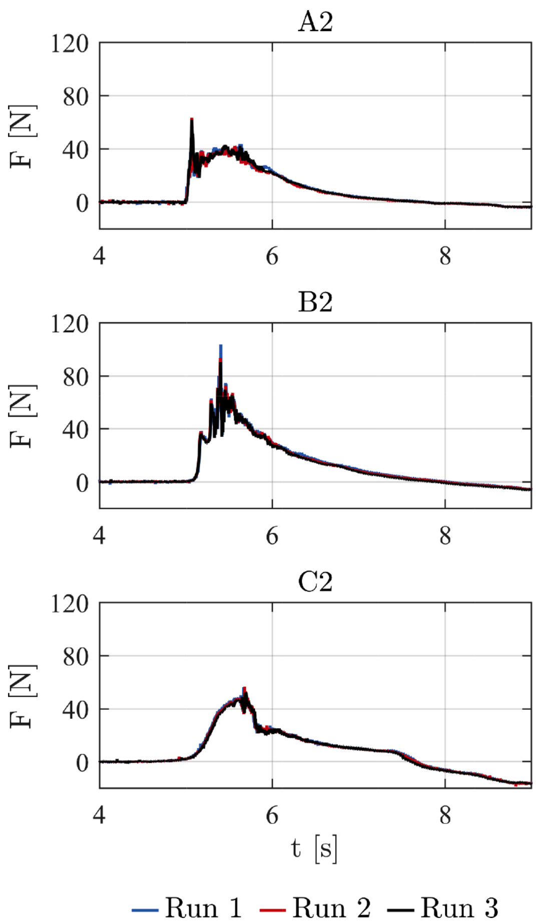

Fig. 7. Repeatability analysis on the M8 global array under wave cases A2, B2 and C2.

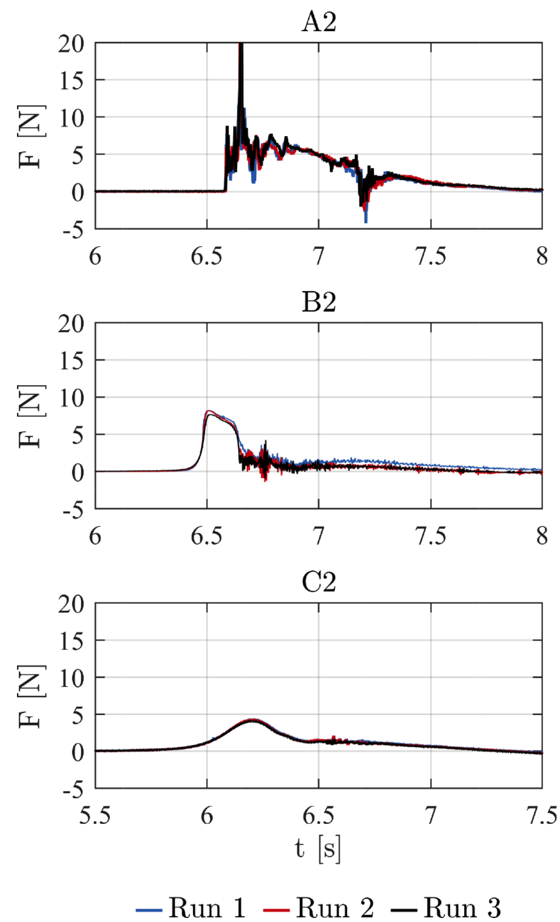

Fig. 8. Repeatability analysis on the M8 individual load block in the front row under wave cases A2, B2 and C2.

the greatest for array M8, as the relative spacing between the blocks is lower.

Kistler Press Force Sensors of Type 9313AA1 were used in this study. These have a maximum measurement range of 5 kN, but are also calibrated for lower ranges. Within the present study, the lower ranges of 50 N and 500 N were chosen for the individual and global loads, respectively. The sensors are piezoelectric, meaning that they are particularly suitable for impulsive loading scenarios. The natural frequency of the load cells exceeds 38 kHz (Kistler, n.d.). Combined with a sampling frequency of 10 kHz, this ensures the accurate capture of any impulsive loading. The accuracy of these sensors has been extensively validated in past studies, for example Ma and Swan (2020a) and Huo et al. (2025).

4. Experimental results

4.1. Repeatability

All wave cases were repeated three times to ensure wide applicability of the results, measuring both the free surface and applied loading in each trial. A representative set of global loading data, under three different wave cases on array M8, is presented in Fig. 7. In addition, local loads measured on the front row of array M8 are provided in Fig. 8. In both figures, it is clear that the repeatability is excellent across all trials.

Fig. 9 (a) displays the local force-time histories recorded at different positions relative to the front of the array. These were measured at the centre of each row of array M8, under wave case B2. The loading results on each row exhibit different shapes and durations, due to the evolution of the incident flow as it moves through the array. These effects are collectively reflected within the global loading results.

In order to provide additional validation of the loading measurements, the individual force-time histories are added and integrated across the number of columns. This is compared to the global force results in Fig. 9 (b). The cumulative individual results generally closely match the corresponding global loads. Small differences can be observed around the peak of the force-time history. These can be attributed to random variations in the magnitude of impulsive loading between trials and across the width of the array. Due to the strong correlation observed elsewhere in the force-time history, and the very different structural dynamic properties of the individual and global loading rigs, the match between the global and cumulative individual loads is taken to be satisfactory.

It is important to note that similar results to those shown in Figs. 7–9 were observed across all arrays and wave cases. Together, the repeatability of the loading measurements and agreement between the global and cumulative individual loads indicate that the experimental setup accurately captures the forces on the structural arrangements.

4.2. Temporal behaviour

The progression and duration of tsunami flows through coastal communities are important considerations when preparing for events. These are examined here through the force-time histories of the arrays.

The progression of the wave fronts through the arrays is tracked using the time at which the loading maximum occurs in each row. These data are presented in Fig. 10; $t_p - t_m$ representing the time elapsed after the maximum load is observed on the first row. Clear linear relationships are visible in categories B (breaking) and C (unbroken). These are consistent across all arrays. This indicates that in these categories, the

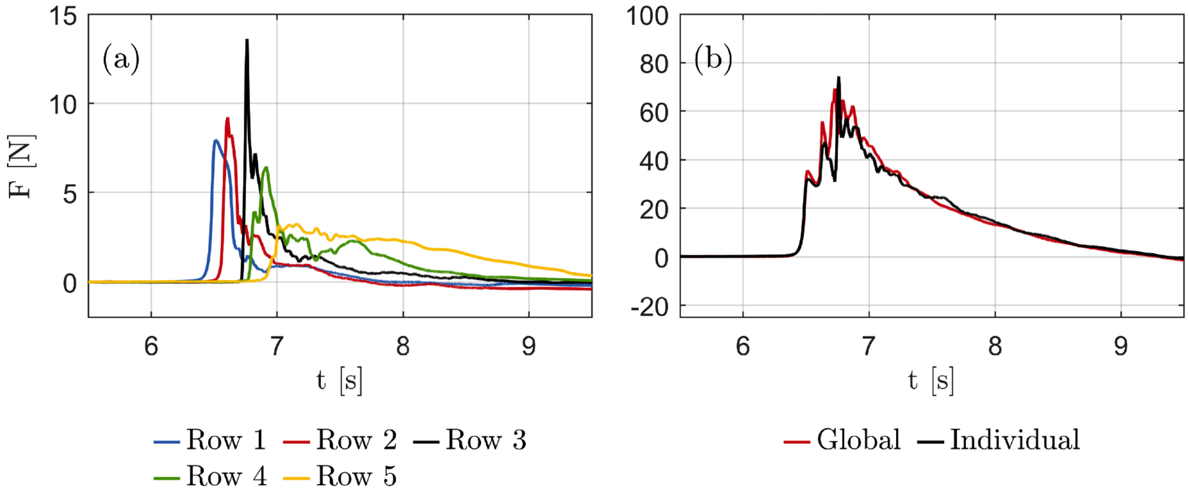

Fig. 9. (a): Loads on rows 1–5 of array M8 under wave case B2. (b): Global and cumulative individual loads.

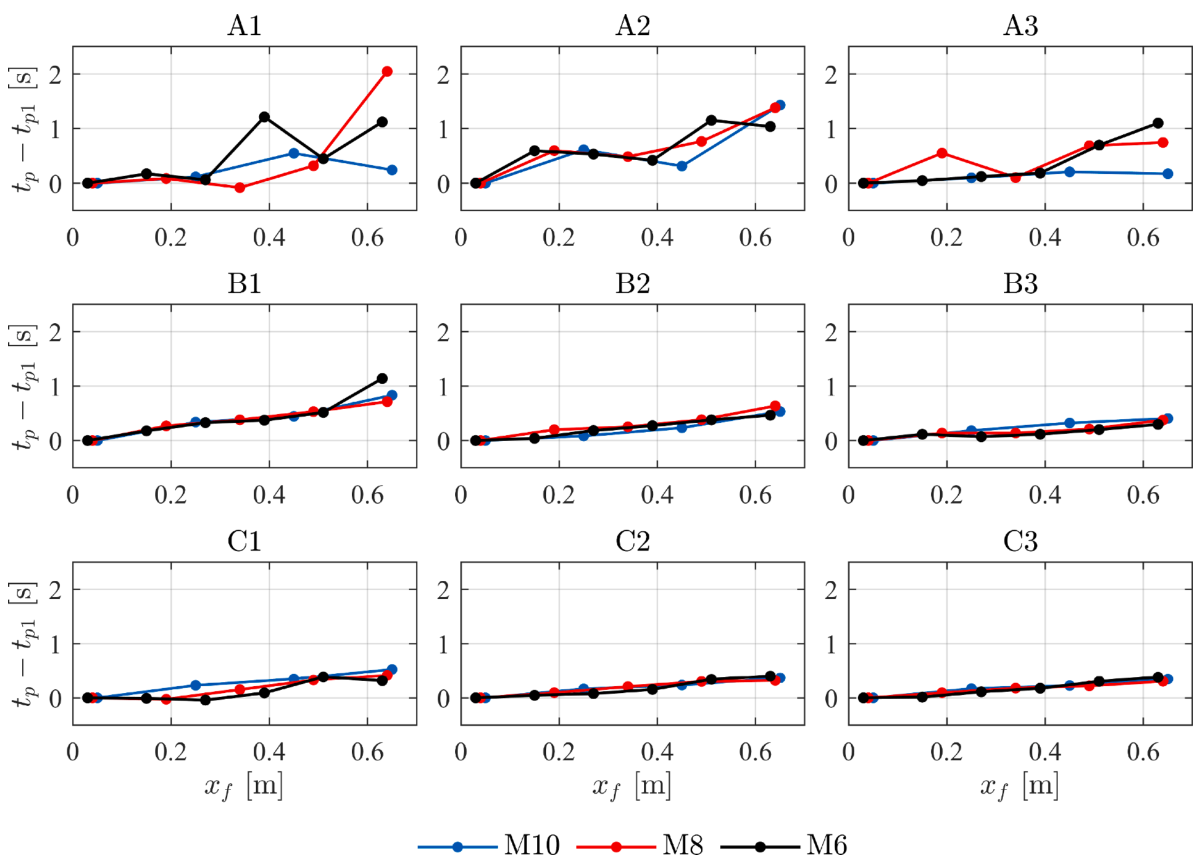

Fig. 10. Time of maximum force at each location within the MRE array relative to the time of maximum force on the first row ($t_p - t_{p1}$), against the distance from the front of the array (x_f), in all wave cases.

propagation of the wave front is not affected by the structural layout or element size. Category A (broken) exhibits less consistent behaviour, with substantial variations across the rows, and differences in behaviour between the arrays. This appears to be random, with no clear relationships visible. This is potentially caused by the uncertain nature of the highly turbulent flows generated by the broken waves.

The present work defines the duration of global loading as the time from the initial rise of global loading from zero to the first point in time at which the global measurements fall below 0. At this point, return flow, the movement of water down the slope, begins to dominate. In adopting this approach, it should be noted that although the duration estimates can be influenced by the lingering fluctuations following the main wave event, these are quickly overcome by the return flow, causing the global loading to 'terminate' (i.e. fall below zero). While the loading durations on the individual blocks may vary, these are considered holistically within the global duration results.

The loading durations are shown in Fig. 11. Within each wave category, the load duration appears to be primarily affected by the wave amplitude. As shown in Table 1, the wave amplitude determines the paddle stroke period, which reduces as wave amplitude rises. Accordingly, across all wave categories, the durations are greatest in the small amplitude cases, where the stroke period is longest.

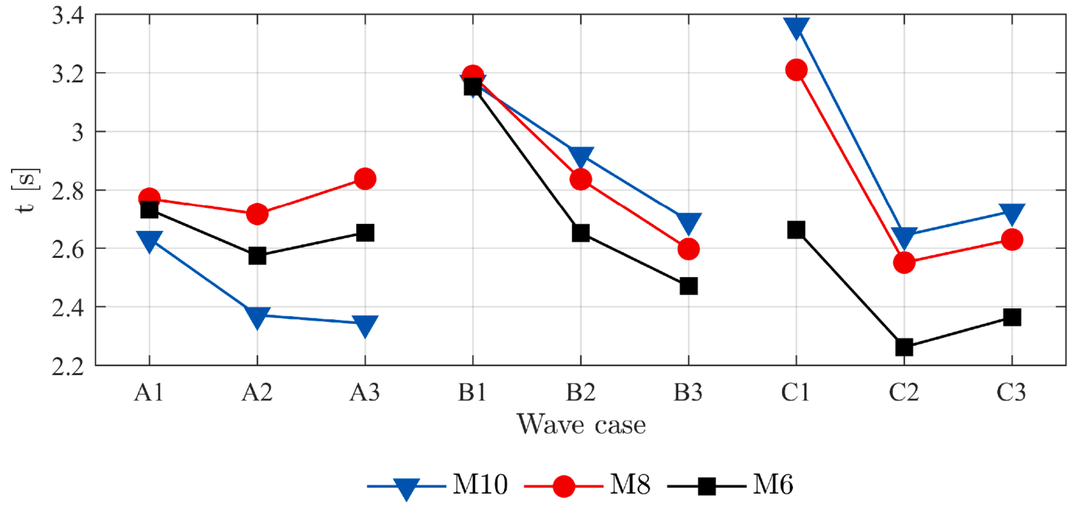

Fig. 11. Durations of global loading, for all wave cases and arrays. Note that the loading durations are primarily affected by the wave period. The role of the structural arrangement is dependent upon the wave breaking conditions.

However, some cases related to A3 and C3 seem to exhibit exceptions to the above trend. The loading durations observed under cases A2 and C2 are typically shorter than those of A3 and C3, respectively. This is in spite of the higher stroke periods in cases A2 and C2. This relationship indicates that a secondary factor is also present, and plays a significant role. The latter is linked to the mechanism of wave breaking. As wave amplitude increases, the wave contains a greater volume of water above the still water level, causing the collapse of the wave to extend over a greater time interval.

Examining the behaviour across different wave categories, the global loading duration generally appears to rise as the position of wave breaking moves towards the rear of the structure. As the position of wave breaking is achieved through increasing the water depth from 500 mm in category A to 600 mm in category C, this means that a level of initial inundation is present prior to the arrival of the incident wave in categories B and C. This causes wave loading to begin earlier, while the wave crest remains further from the MRE array.

Furthermore, within categories B and C, the loading duration is directly related to element size, and lower element size/structural volume results in shorter loading intervals. This is expected, as the smaller arrays cause less disturbance in the flow, allowing faster propagation and reducing loading duration.

Category A exhibits a different relationship. Here, the durations are lowest in array M10 and greatest in array M8, across all wave amplitudes. This can be attributed to the properties of the structural arrangements. As shown in Table 2, array M10 has the greatest frontal area ($A_f = 300\text{cm}^2$). This may serve to reduce penetration of water into the array, and hence limit the loading duration. Arrays M8 and M6 have lower A_f, allowing more water to enter the structural arrangement. Array M8 has the greatest plan area ($A_p = 1280\text{cm}^2$). This may act to capture water during the inundation process and therefore extend the duration of loading.

The experimental results demonstrate that where waves break amid or after the structural arrangement, increasing the element size and volume of the array causes tsunami loading to take place over a greater interval, due to their greater disruption of the flow. Where waves break before the arrangement, the loading duration is not explicitly linked to element size alone, and other properties of the array play an important role.

4.3. Loading

The experimental apparatus was designed to measure the global forces on MRE arrays, and the loads applied to individual elements within these. The individual forces provide useful insight on the design loading of critical infrastructure, allowing examination of the importance of the position of a structure relative to others under different wave conditions. In contrast, the global loading results supply information on the interaction between the tsunamis and arrangements (e.g. neighbourhoods or city blocks). This enables holistic consideration of the flow behaviour and the role of structural layout and size.

The maximum global loads are shown in Fig. 12. The maxima increase with wave amplitude within each wave category. As the wave amplitude rises, the stroke period reduces and the steepness of the wave increases. Accordingly, greater mass-flux and particle velocities are present, resulting in an increased rate of momentum transfer when the waves interact with arrays.

While the loads are similar in magnitude across all wave categories, those measured in category B are typically greatest under similar conditions. This is caused by the breaking position. Breaking is closely associated with extreme loading in the design of coastal and offshore infrastructure, due to the large particle velocities that occur (Cuomo et al., 2010). The breaking process also rapidly dissipates large amounts of energy through air entrainment and turbulent motion, and hence distance from any breaking activities reduces the applied forces. In category B, where the waves break amid the structures, the array experiences the greatest velocities and there has been no opportunity for dissipation prior to the array.

In all wave categories, the global loads increase as the size of the structural arrangement rises. However, the differences with structural arrangement increase in magnitude as the position of wave breaking moves further up the slope. In category A, the greatest percentage difference betwen M10 and M6 is approximately 17 %. In category B, this rises to 32 %, while in category C, it reaches 49 %. This is because, as the water depth and initial inundation increases, the proportion of volume that is initially submerged increases more rapidly for the smaller arrays. As such, they cause less disturbance to the incident wave and experience lower global loads.

The trends visible in the global loading data are supported by the local loading results. As shown in Fig. 13, the maximum individual loads are generally similar in magnitude across all wave categories. All structural arrangements exhibit comparable spatial behaviour, and the magnitude of the forces increases with wave height and element size. Impor-

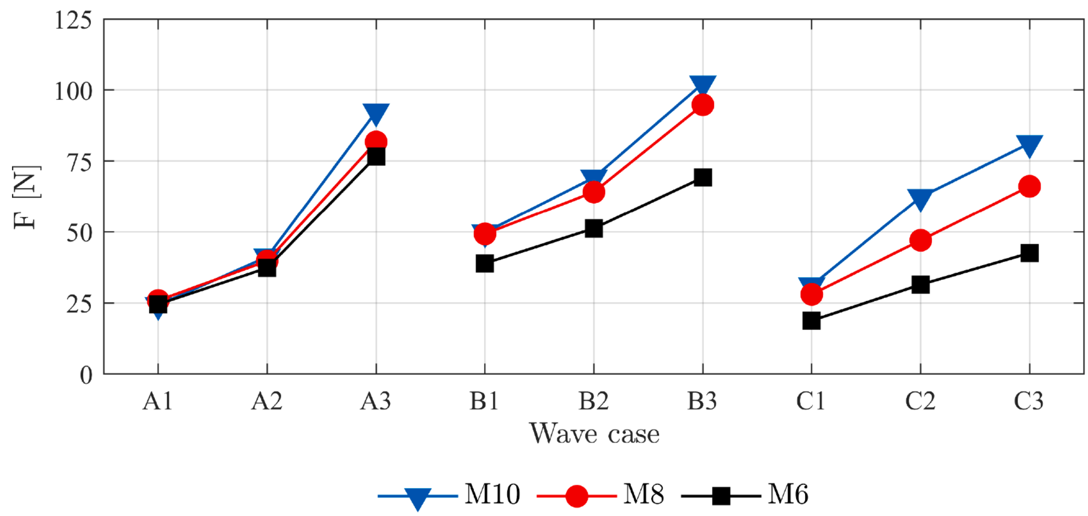

Fig. 12. Maximum global forces, for all wave cases and arrays. Note that the forces increase with wave height and the size of the structural arrangement, and that the importance of the structural arrangement is dependent upon wave breaking conditions.

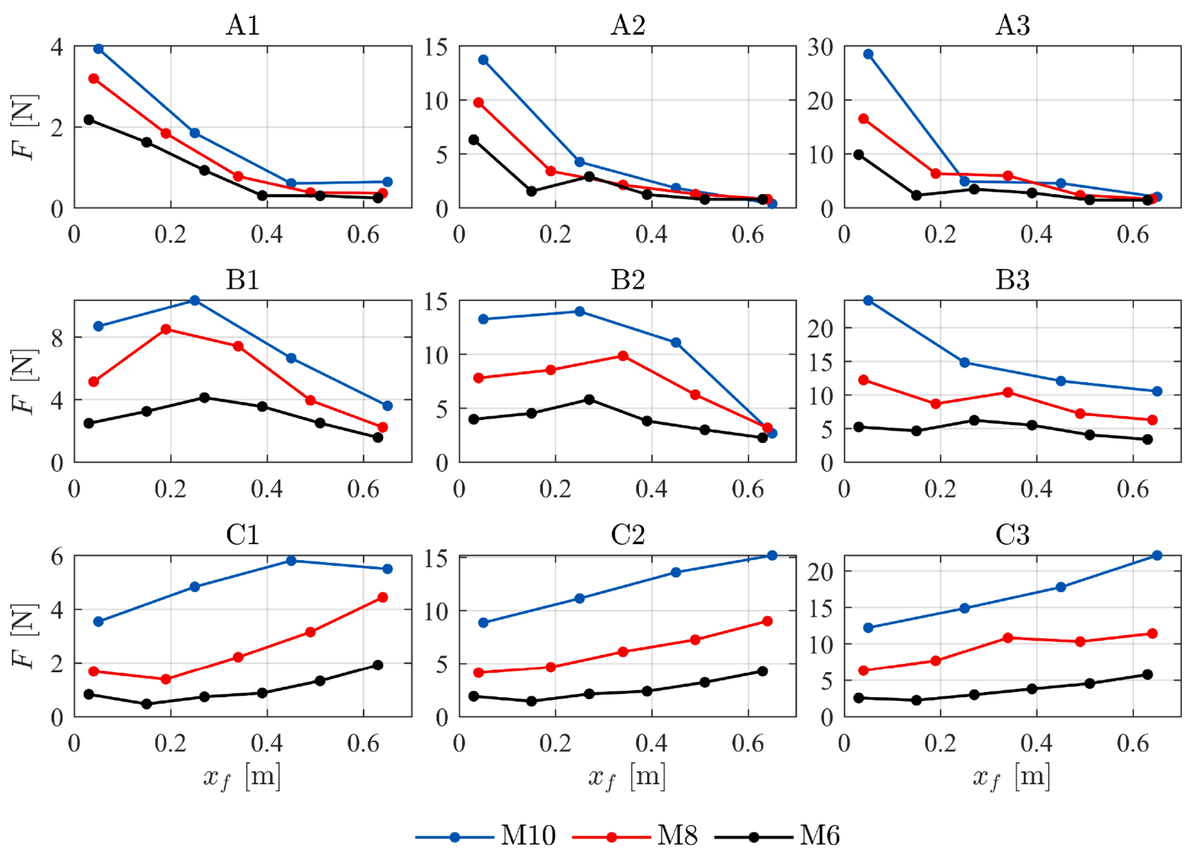

Fig. 13. Maximum force at each location throughout the loading rig, under all wave cases. $x_f = 0$ is the front of the loading rig, and $x_f = 0.7$ is the rear.

tantly, however, the location where the maximum force occurs varies significantly between wave categories.

In category A (broken), the loads drop significantly after the first rows before plateauing towards the rear of the array. Within category B (breaking), cases B1 and B2 experience the greatest loads near the centre of the arrays, while the highest load in case B3 occurs in the front row. The wave loads then fall towards the rear of the array, but remain at a higher level than those observed in category A. Finally, in category C (unbroken), the wave loads increase at positions towards the rear of the array.

These observations demonstrate that the point of breaking determines the location of the maximum load. Breaking occurs prior to the array in category A, at the front of the array in case B3, in the middle for B1 and B2, and behind the array in category C. Within Fig. 13, the shielding of structures in the rear by those in front is most apparent in categories A and B, after the point of wave breaking. In particular, for category A, the loads fall significantly behind the first 1–2 rows. The results in wave case A1 and across category B are in agreement with the 40 % to 70 % decrease estimated by Tomiczek et al. (2016). In cases A2 and A3, the reduction in force exceeds this range, falling between 60 % and 85 % after one row.

In contrast, no evidence of a shielding effect is present in category C. The loads progressively increase in magnitude towards the rear, as the waves steepen and approach breaking. The existence of multiple rows of aligned seaward structures does not, in this case, result in lower loads on the rearmost structures.

Taking all results together, smaller structural arrangements typically experience loading for shorter time intervals, except where waves break before the array. The duration of loading is influenced primarily by the wave amplitude and associated period. The form of wave breaking also plays a role, and acts to increase loading duration in the highest-amplitude waves. In cases that break before the array, the wave front progresses unsteadily through the structural arrangement, due to their highly turbulent nature. Where breaking occurs within or after the arrangement, the temporal propagation of the wave front appears undisturbed. The form of structural arrangement does not influence the advance of the wave front.

In contrast, the element size of the structural arrangement has a clear effect on the magnitudes of the global and individual loads. Larger differences occur as the position of wave breaking moves up the slope, and initial inundation increases. The location of the greatest load within the arrangement is determined by the position of wave breaking. Shielding effects are only observed after wave breaking occurs. Where wave breaking occurs behind the array and the initial inundation is large, the magnitude of the forces increases towards the rear of the array.

5. Numerical modelling

5.1. SWASH simulations of incident wave conditions

In order to generate the necessary free-surface and kinematics inputs for ASCE 7, MLIT 2570, and the LMA model (including behaviour during and after breaking), the wave flume was first modelled using SWASH (Zijlema et al., 2011), an open-source non-hydrostatic wave-flow model. The key advantages of SWASH in this study are its theoretical validity in shallow waters, its rapid computation of the surface elevation and kinematics, and rigorous control over their discretisation. It serves as an initial estimate which is refined further in Section 5.3.

SWASH is founded upon solution of the non-linear shallow water equations, describing the mass and momentum balance for an incompressible fluid with a free-surface (Zijlema et al., 2011; Smit et al., 2013). It is a well established model, validated for a wide range of applications (see Smit et al., 2013, Smit et al., 2014, Rijnsdorp et al., 2014, Suzuki et al., 2017 and Rijnsdorp et al., 2022). Recently, Al Khalili et al. (2025) used SWASH to provide comparisons to waves generated in the same flume as the present study. While this study demonstrates that SWASH is generally able to recreate the macro-scale effects of wave breaking on wave height, the description of breaking wave hydrodynamics in SWASH and similar models is inherently challenging, due to simplifications in the modelling of physical effects such as air entrainment, turbulence and overturning. Further description of how SWASH represents wave breaking is provided by Zijlema et al. (2011), Smit et al. (2013) and Al Khalili et al. (2025).

Following the approach presented by Al Khalili et al. (2025), 2D simulations were carried out in this study. A mesh size of approximately 300 points per wavelength was adopted. A Sommerfeld radiation condition at the beach end of the numerical domain was implemented to minimise reflections at the outflow boundary. A weakly reflective boundary condition was imposed at the generating boundary to absorb any (small) reflected energy from the beach. Friction was modelled through a Manning coefficient of $0.019\,\mathrm{m}^{-1/3}\mathrm{s}$, and viscosity was incorporated through vertical mixing only, using the $k-\epsilon$ model. The breaking parameters were kept as the default values of $\alpha = 0.6$ and $\beta = 0.3$. The time series

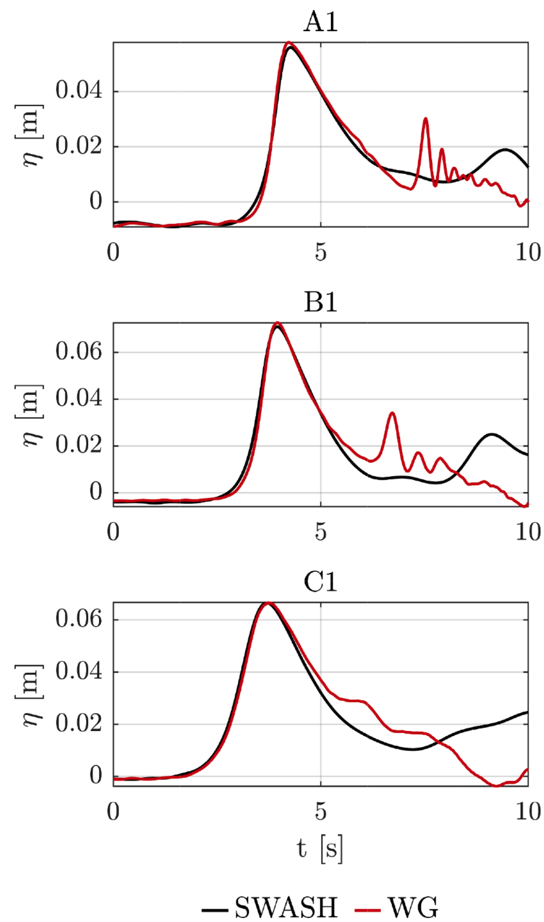

Fig. 14. Comparison of numerically simulated surface profiles from SWASH and experimental measurements at the final wave gauge, for wave cases A1, B1 and C1.

at the first laboratory wave gauge was used as input to the numerical wavemaker. The model did not include any structures and hence provides undisturbed surface elevations and kinematics.

The numerical domain was discretised into 22 vertical layers. The four uppermost layers constituted 1, 2, 3 and 4 % of the water depth respectively. The remaining layers were uniformly 5 % of the water depth. This dense scheme was selected to provide detailed information on wave kinematics. The reader is directed to Appendix C for the SWASH configuration files used in this study.

In order to evaluate the performance of SWASH and minimise potential errors in the loading estimates, surface elevations were compared to the experimental results at the final wave gauge. Two rounds of iterations were carried out to match the numerical and experimental wave heights at the final gauge. Fig. 14 displays the resulting surface elevations for the small amplitude waves within each category. This shows that SWASH recreates the surface profile of the primary ERF wave well, with a strong match in both the wave amplitude and the wave shape. Differences are apparent for the following wavetrain. However, this is not relevant to the focus of this study, as it occurs after the primary ERF wave and main loading event, and as such was not investigated further.

5.2. Loading predictions using SWASH input

The surface elevation and kinematics results from SWASH were used as input to LMA, MLIT 2570 and ASCE 7–22. In LMA, the outputs were linearly interpolated at a vertical and horizontal spacing of $0.1\,\mathrm{mm}$ to produce the momentum parcels. While it is capable predicting the load-

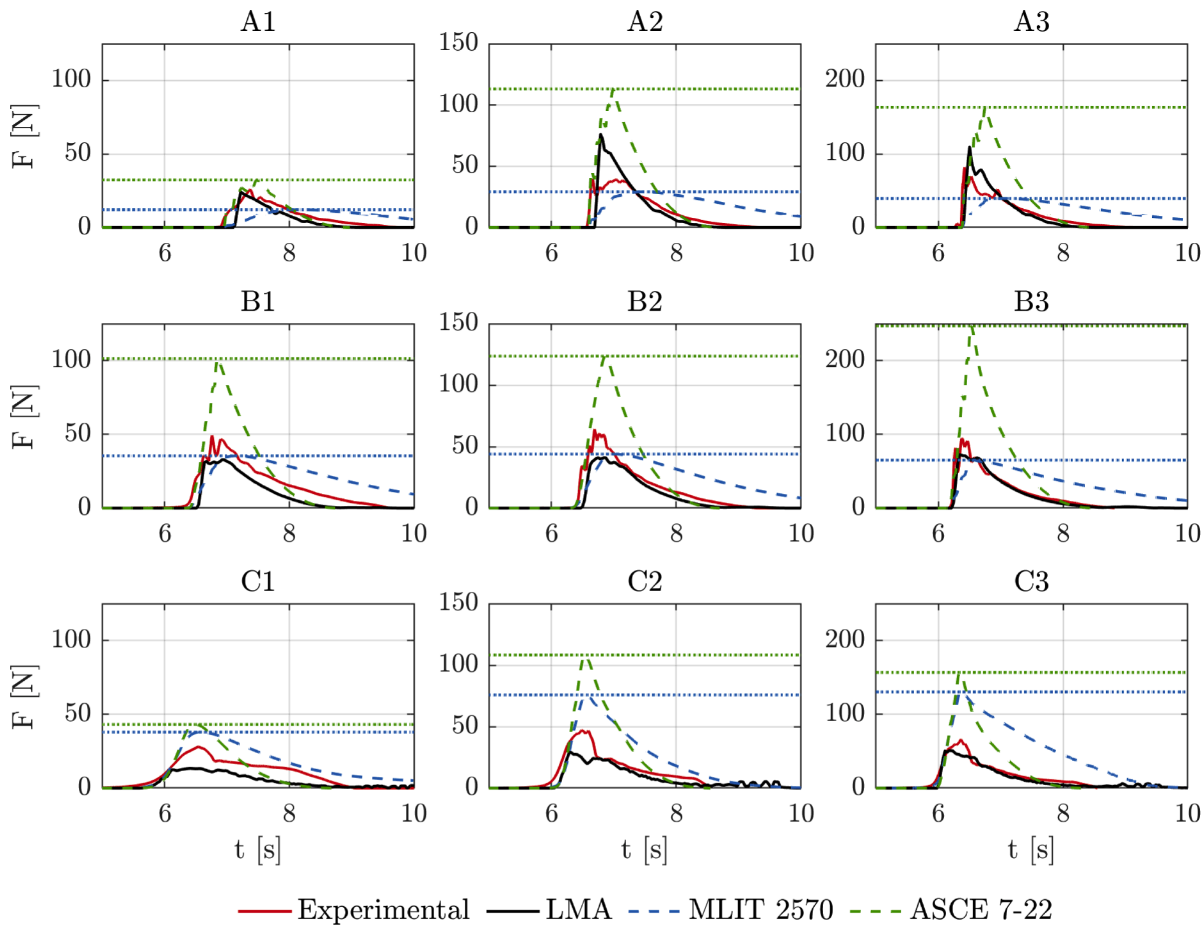

Fig. 15. Comparison of global experimental measurements and LMA predictions using SWASH, for array M8. Maxima of MLIT 2570 and ASCE 7–22 predictions are identified by dotted lines.

ing on individual elements, in this study the global loading was determined using bulk properties to demonstrate the feasibility of the method. Due to the strong correlation between the measured global and individual loads, as shown in Fig. 9, accurate recreation of the global loads indicates that the loading model is capturing the physical processes accurately. In this case each row of the arrays was modelled as a single sponge component. The porosity was set as the ratio of structural volume. For example, each row of the M10 array has a cumulative structural volume $V_b = 300\,\mathrm{cm}^3$, within a gross volume $V_g = 600\,\mathrm{cm}^3$. Accordingly, the porosity of each row $p = (V_g - V_b)/V_g = 0.5$. Higher porosity values indicate that there is less structural volume present, and are therefore associated with lower dissipation of momentum. Other than a physical estimate of the porosity as demonstrated herein, there is no other parameter to define.

MLIT 2570 and ASCE 7–22 were implemented to estimate the loads on individual blocks in each row using Eqs. (4) and (5) respectively. The individual results were then superimposed and integrated across the number of columns to predict global forces. It should be noted that in their original forms, both models do not consider the temporal variation of the wave and provide estimates for the maximum force exerted throughout inundation. This is typically the key point of interest and there is often insufficient temporal information on the incident wave. In this study, the numerical simulations provide the time histories of free surface elevation and kinematics. As such, when generating estimates using MLIT 2570 and ASCE 7–22, the instantaneous numerical wave heights and kinematics at the front of each block were applied at each time step. This improvement provides full loading time-histories for both methods. In Categories B and C, the initial inundation exerts balanced hydrostatic loading on the MREs. The additional force introduced by the wave was therefore estimated using the wave height above the still water level. However, to reflect the fact that a greater proportion of the block is submerged, the loads were integrated from bed level to the top of the block, or the wave height if this falls below the top of the block.

When applying ASCE 7–22, the velocity of the flow was taken as the mean velocity across the depth of the block. The water depth coefficient a and tsunami importance factor I_{tsu} were set equal to 1 to enable more accurate comparison to the experimental results. This approach would not be the case in practical design scenarios, where conservatism is desirable. As this study seeks to assess the underlying accuracy of the methods, the coefficients are ignored. Considering the application of Eq. (5), the drag coefficient $C_D = 2$, as recommended in ASCE (2021) for square structures.

The force-time histories predicted by LMA, MLIT 2570 and ASCE 7–22 are compared to the experimental measurements on array M8 in Fig. 15. A complete account of the representative error statistics is provided in Table B.4 in Appendix B. Examining first MLIT 2570, this prediction method significantly overestimates the duration of the loading. The water level remains high after the primary wavefront has passed, due to return flow down the slope. Although the net velocity in this phase is seaward, this is not incorporated within the hydrostatic formulation. In category A, MLIT 2570 underestimates the maximum forces by up to over 50 %. The margin of error reduces in category B to around 30 %, though the predictions remain low relative to the measured forces. This is not the case in category C, where MLIT 2570 significantly overpredicts the applied loads. The differ-

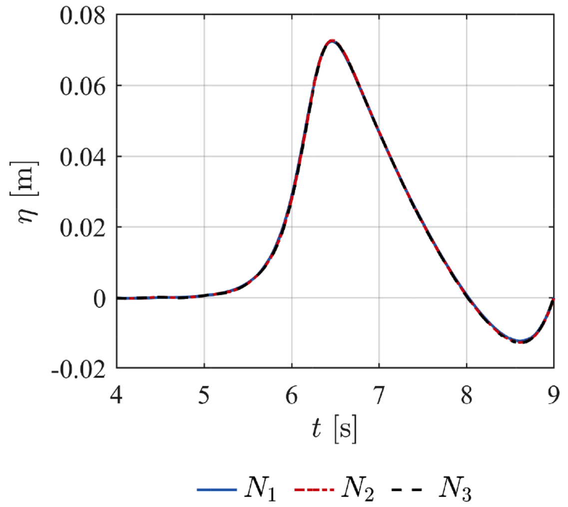

Fig. 16. Comparison of OpenFOAM surface elevation of wave case B2 at $x = 13.4m$ using $N_1 = 70000$, $N_2 = 105000$, and $N_3 = 280000$ cells.

ence increases as wave height rises, reaching approximately 100 % in case C3.

Considering ASCE 7–22, the predicted loading durations are much more realistic than MLIT 2570, though consistently slightly shorter than the laboratory measurements. The shape of the force-time histories appear more representative, but the large differences in magnitude in categories B and C make exact comparisons challenging. In all categories, ASCE 7–22 significantly overpredicts the applied loads. This is more severe in categories B and C, where the predicted loads exceed the measured by over 100 % in cases B3 and C3.

Finally, the LMA estimates are of the same order of magnitude as the experimental results. This is particularly true for wave cases A1, A3, B1 and B3, where the force-time histories are recreated relatively accurately. In general, LMA appears to perform relatively well in predicting the overall shape of the force-time histories and the loading duration, producing significantly more accurate estimates than ASCE 7–22 and MLIT 2570 in all cases. Agreement is less good for category C, where wave breaking occurs behind the structural arrangement. Considering the loading maxima in this category, the LMA results are within 25 % of the experimental measurements in case C3, and 55 % in cases C1 and C2.

It is evident that, when applied using SWASH estimates of the free surface elevation and kinematics, LMA performs better than ASCE 7–22 and MLIT 2570. However, there still remains room for significant further improvement. A possible cause of error in the model predictions is insufficiently accurate modelling of the incident wave. For example, Ma and Swan (2020b) accurately predicted the wave-in-deck loading on topside structures using LMA, when applying a fully nonlinear boundary element method calculations to recreate non-breaking waves. In this study, SWASH was used to produce initial estimates of the behaviour of the breaking waves. As identified throughout Section 4, breaking dominates the wave loading results. However, SWASH only approximately captures the breaking behaviour. This is the probable cause of the large differences between the model predictions and the experimental results observed in Fig. 15.

5.3. OpenFOAM simulations of incident waves

In order to further investigate the source of inaccuracy within the load predictions made in Section 5.1, the waves in category B were reproduced using OpenFOAM (Weller et al., 1998), an open source Computational Fluid Dynamics (CFD) software. This modelling suite has been employed in several prior investigations of tsunami behaviour, including Dimakopoulos et al. (2014) and Larsen and Fuhrman (2019). OpenFOAM is capable of accurately recreating physical behaviour and is often used in studies of wave breaking (see Chenari et al. (2015) and Jiang et al. (2022)) However, this comes at significantly greater computational cost than the SWASH simulations.

The OpenFOAM simulation follows setup guidelines set out by Kasiman (2017). A structured 2D rectangular mesh was generated throughout the domain. The full volume of the flume was modelled. An 8-times refinement was applied between 2.5 cm below the front of the loading rig and 20 cm above the still water level. The vertical extent of this band is such that it covers the entire crest-to-trough zone that contains the free surface. A mesh convergence test was carried out to determine the optimal base mesh size. Three meshes of base size 5 cm, 3.75 cm and 2.5 cm were examined. These meshes had approximately $N_1 = 70000$, $N_2 = 105000$, and $N_3 = 280000$ cells respectively. The results indicated that surface profiles were satisfactorily reproduced using $N_1 = 70000$ cells, as shown in Fig. 16.

Waves were generated on the input boundary using the Waves2Foam toolbox, which is shown to accurately model the free surface of waves by Jacobsen et al. (2012). This used the frequency spectra created for the experimental wavemaker. Truncations were applied to accelerate the numerical simulations, where only the 200 components of greatest amplitude were considered. The free surface elevations were reproduced to a similar level of accuracy as those shown in Fig. 14. Due to the strong matches in the loading profiles, displayed in Fig. 17, the simulations were deemed acceptable.

Adopting a consistent approach with that applied using SWASH, the numerical wave amplitudes were iterated to match the experimental values at the final wave gauge. Turbulence was incorporated through the linear compressible $k - \epsilon$ Reynolds-averaged simulation model. Comparison to alternative models, including linear incompressible $k - \epsilon$ and nonlinear $k - \epsilon$, produced only minor differences. The OpenFOAM simulations were run until the primary wave front had fully passed through the array, to minimise the simulation time. The reader is directed to Appendix C for the OpenFOAM configuration files used in this study. The LMA, MLIT and ASCE characteristics described in Section 5.1 were unchanged.

5.4. Force prediction using OpenFOAM input

The experimental and predicted force time-histories for all structural arrangements are displayed in Fig. 17, while a breakdown of error statistics is provided in Table B.5 in Appendix B. Examining the predictions of MLIT 2570, the force predictions do not return to zero in all cases. This is caused by the termination of the OpenFOAM simulations after the primary wavefront. The loading durations remain significantly overestimated in the M6 array, but are more realistic in the M8 and M10 arrays. The predicted force-time histories are generally much closer in magnitude to the experimental results than in Fig. 15, and in arrays M6 and M8, the peak loads are accurately predicted in cases B1 and B2. However, in the M10 array, differences of up to 50 % are still present.

The ASCE 7–22 predictions also improve greatly with the OpenFOAM inputs. The predictions typically recreate the experimental results well in shape and magnitude. Larger errors are observed in several cases - ASCE 7–22 overestimates the maximum forces in case B1 in array M6 by 55 %, and cases B1 and B2 in array M8 by approximately 40 %. However, the predictions remain far superior to those displayed in Fig. 15 and are more consistent than those from MLIT 2570.

Finally, the LMA and experimental values are much more closely aligned than those shown in Fig. 15. They generally match well in magnitude and shape. The experimental durations slightly exceed the numerical, with the disparities largest in case B1 in all arrays. The greatest differences in magnitude are also present in this case in arrays M8 and M10. Comparing the maximum forces, the level of accuracy varies slightly between arrays. In all cases, the results are within 26 % of the experimental values, decreasing to within 10 % in cases B2 and B3 in arrays M6 and M8, and case B1 in array M10.

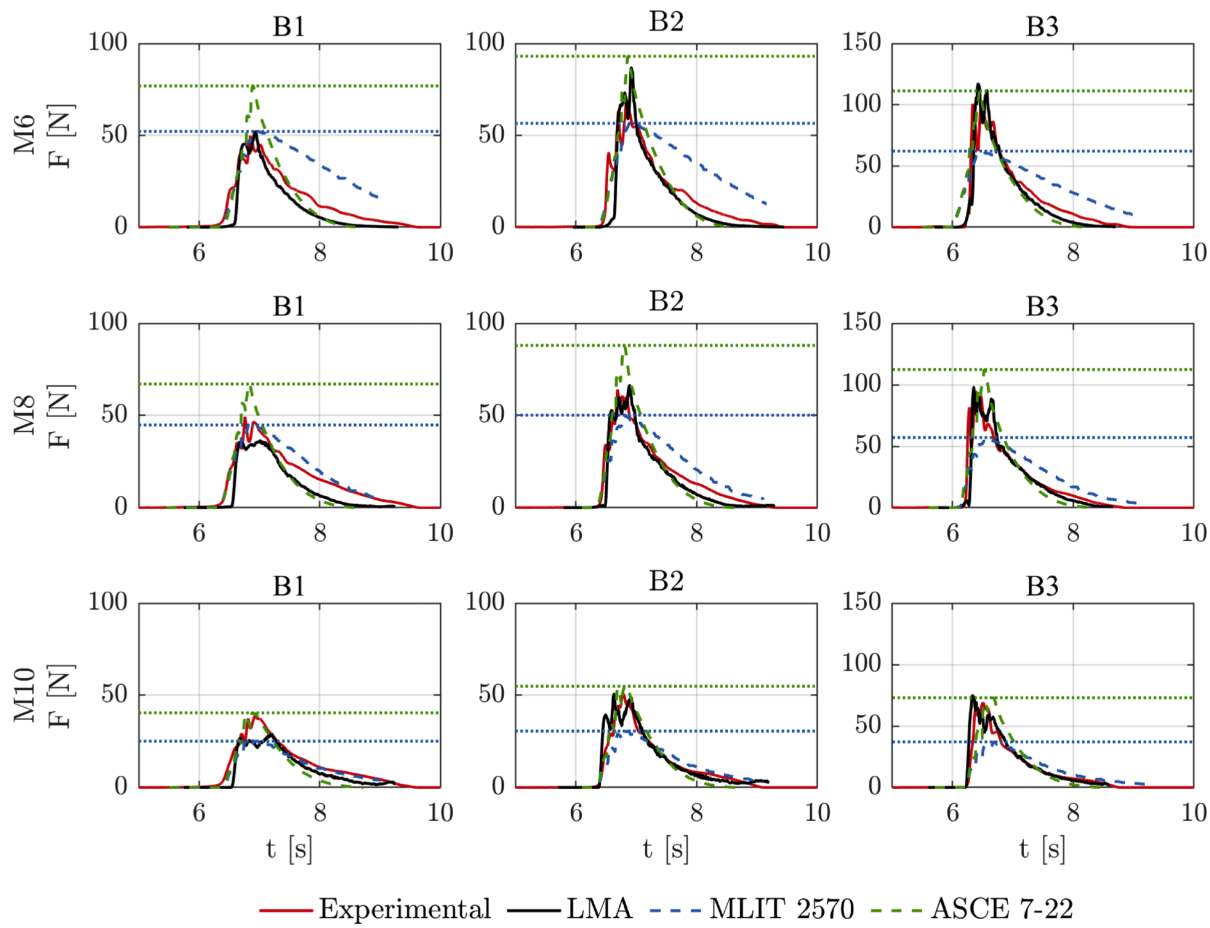

Fig. 17. Comparison of global experimental measurements and LMA predictions using OpenFOAM, for category B waves across all arrays. Maxima of MLIT 2570 and ASCE 7–22 predictions are identified by dotted lines.

In summary, this section has investigated the effectiveness of MLIT 2570, ASCE 7–22 and a Lagrangian Momentum Absorption scheme for the prediction of global tsunami loads on three structural arrangements. SWASH was used to generate initial comparisons, due to its rapid calculation and simple implementation. SWASH and LMA present acceptable results in some cases, followed in accuracy by ASCE. However, it is clear that differences to the experiments are significant. In order to identify the cause, refined inputs were generated using OpenFOAM. This enabled greater accuracy in all prediction methods. In particular, ASCE 7–22 and LMA accurately recreate the experimental force-time histories and peak loads. This demonstrates that both methods are capable of accurately estimating the tsunami wave loads on coastal communities. It is important to note that the predictions are highly dependent upon the accuracy of wave modelling inputs. In general, LMA requires no empirical input and appears to be more consistent and less susceptible to the uncertainties within the wave modelling. This is unsurprising as the model is based on a more physically realistic formulation where the incident wave momentum is gradually dissipated. Across the board, further refinement of the OpenFOAM simulations would likely to further improve the accuracy of the loading predictions.

6. Conclusion

This study presents the results of an experimental investigation into tsunami wave loading on three arrangements of macro-roughness elements. The local forces on individual elements and the global forces on the arrangements at city block scale are presented and analysed. The laboratory measurements are then used to validate the loading predictions of a momentum-flux model.

Considering first the experimental results, the duration of loading is dependent upon the form of the structural arrangement. The location of wave breaking determines which structural properties influence the loading duration. In contrast, the progression of the wave front through the array is not influenced by the form of the structural arrangement.

The magnitude of the applied load is dependent upon element size, and the relative importance of structural volume increases as the location of wave breaking moves up the slope. The position at which the maximum load occurs within the array is defined by the location of wave breaking. Shielding effects are only observed after wave breaking has occurred, and structures at the rear of the arrangement do not always experience lower forces.

Through comparison to the experimental results, the effectiveness of theoretical predictions from MLIT 2570, ASCE 7–22 and a momentum-flux numerical scheme (LMA) was investigated. The results demonstrate that both ASCE 7–22 and LMA are capable of predicting the global loads on structural arrangements to a reasonable level of accuracy, when provided with suitable estimates of wave surface profile and kinematics. In this study, free-field simulations generated using OpenFOAM were found to be more appropriate than those carried out using SWASH. Whilst all models are affected by the accuracy of the wave inputs, LMA is found to be more robust than both ASCE 7–22 and MLIT 2570. In comparison to the design codes, LMA presents a more physics-based approach and has the potential of being a more generally applicable model. This can potentially help to remove uncertainties related to the prediction of design loads, especially those related to the choice of empirical coefficients, as the latter are subject to effective calibration. While it has only been applied to the prediction of global tsunami loads here, it is sufficiently flexible to also determine the loads on individual structures and structural elements, as required for engineering design. In order to comprehensively demonstrate the effectiveness of the model, further analyses are required across a broader range of structural scenarios and incident wave conditions.

CRediT authorship contribution statement

Oliver Millar: Writing - original draft, Visualization, Methodology, Investigation, Formal analysis, Data curation; **Li Ma:** Writing - review & editing, Supervision, Project administration, Methodology, Conceptualization; **Ioannis Karmpadakis:** Writing - review & editing, Supervision, Project administration, Methodology, Conceptualization.

Data availability

Data will be made available on request.

Declaration of competing interest

The authors declare that they have no known competing financial interests or personal relationships that could have appeared to influence the work reported in this paper.

Acknowledgements

The authors are grateful to Vasileios Bellos for his assistance in preparing the error function waves, Xinlu Mao for her support in setting up the experimental apparatus, Umniya Al-Khalili for her guidance on the SWASH model, and Chong Huo for his advice on the OpenFOAM simulations. They also acknowledge Chris Swan for his key role in conceptualising this work and in the early stages of delivery.

Appendix A. Scaling factors

Table A.3
Froude similarity scaling factors (λ) for length (L), time (t), area (A), volume (V) and force F. λ is the ratio of prototype to laboratory dimensions.

	L [m]	t [s]	A [m^2]	V [m^3]	F [N]
λ	100	10	10^4	10^6	10^6

Appendix B. Table of results

This appendix provides the key error statistics for the global loading predictions from LMA, ASCE 7–22 and MLIT 2570. This considers the percentage difference between the maximum forces

$$PD = 100\frac{F_{theo} - F_{exp}}{F_{exp}}, \tag{B.1}$$

and the root mean squared error (RMSE) for each force-time history.

Appendix C. Data availability

The configurations and codes necessary to reproduce the SWASH and OpenFOAM simulations presented in this study are freely available at the online repository: https://github.com/ic-civil-fluids/tsunami_loading

Table B.4
Percentage difference between maxima (PD) and RMSE between experimental measurements and predictions using SWASH inputs, for array M8 under all wave cases.

	ASCE 7–22		MLIT 2570		LMA	
Case	PD	RMSE	PD	RMSE	PD	RMSE
A1	25.01	4.13	-53.07	8.14	-6.22	4.23
A2	184.20	26.89	-26.62	14.96	91.17	11.81
A3	99.86	39.39	-51.64	21.83	33.75	12.60
B1	105.67	18.56	-28.09	11.83	-33.45	8.23
B2	92.60	25.82	-31.50	17.11	-35.98	8.37
B3	160.18	60.34	-31.47	26.35	-23.66	8.62
C1	53.93	8.54	35.49	8.97	-52.26	8.07
C2	130.06	26.71	61.15	20.64	-37.08	8.84
C3	136.95	33.22	97.19	51.68	-23.03	6.49

Table B.5
Percentage difference between maxima (PD) and RMSE between experimental measurements and predictions using OpenFOAM inputs, for cases B1 to B3 across all arrays.

		ASCE 7–22		MLIT 2570		LMA	
Array	Case	PD	RMSE	PD	RMSE	PD	RMSE
M6	B1	54.43	9.75	4.75	16.23	4.62	7.73
	B2	34.47	9.39	-18.26	16.43	25.39	9.83
	B3	8.78	13.15	-39.22	18.62	14.40	12.96
M8	B1	36.09	10.00	-8.98	4.34	-26.05	8.32
	B2	37.18	8.83	-21.73	8.02	3.38	6.27
	B3	18.48	12.71	-39.83	14.72	3.24	11.58
M10	B1	4.00	5.89	-35.55	5.41	-25.89	6.03
	B2	7.17	4.44	-40.32	6.62	-1.12	5.25
	B3	5.46	10.36	-46.49	12.78	8.07	8.50

References

Aknin, D., Spinneken, J., 2017. A laboratory investigation concerning the superharmonic free wave suppression in shallow and intermediate water conditions. Coastal Eng. 120, 112–132. https://doi.org/10.1016/j.coastaleng.2016.11.015

Al Khalili, U., Karmpadakis, I., Christou, M., Bellos, V., et al., 2025. Performance of SWASH in modelling regular and irregular waves on mild bathymetries. Coastal Eng. 199, 104745. https://doi.org/10.1016/j.coastaleng.2025.104745.

Almalki, Y.R., Swan, C., Karmpadakis, I., 2025. Experimental investigation of pile-supported oscillating water column devices. Renew. Energy 248. https://doi.org/10.1016/j.renene.2025.122973

Arnason, H., Petroff, C., Yeh, H., 2009. Tsunami bore impingement onto a vertical column. J. Disaster Res. 4 (6), 391–403. https://doi.org/10.20965/jdr.2009.p0391

ASCE 7–22, 2021. Minimum design loads and associated criteria for buildings and other structures. American Society of Civil Engineers. https://doi.org/10.1061/9780784415788

Baldock, T.E., Cox, D., Maddux, T., Killian, J., Fayler, L., 2009. Kinematics of breaking tsunami wavefronts: a data set from large scale laboratory experiments. Coastal Eng. 56, 506–516. https://doi.org/10.1016/j.coastaleng.2008.10.011

Baldock, T.E., Peiris, D., Hogg, A.J., 2012. Overtopping of solitary waves and solitary bores on a plane beach. Pro. Royal Soc. A 468, 3494–3516. https://doi.org/10.1016/j.coastaleng.2008.10.011

Chanson, H., 2005. Analytical solution of dam break wave with Flow resistance: application to tsunami surges. In: Proceedings of 31st IAHR Biennial Congress. Korea Water Resources Association, Seoul, Korea, pp. 3341–3353.

Chenari, B., Saadatian, S.S., Ferreira, A.D., 2015. Numerical modelling of regular waves propagation and breaking using waves2foam. J. Clean Energy Technol. 3, 276–281. https://doi.org/10.7763/JOCET.2015.V3.208

Chinnarasri, C., Thanasisathit, N., Ruangrassamee, A., Weesakul, S., Lukkunaprasit, P., 2011. The impact of tsunami-induced bores on buildings. Maritime Eng. 166 (MA1), 14–24. https://doi.org/doi.org/10.1680/maen.2010.31

Chock, G.Y.K., 2016. Design for tsunami loads and effects in the ASCE 7–16 standard. J. Struct. Eng. 142 (11). https://doi.org/10.1061/(ASCE)ST.1943-541X.0001565

Cuomo, G., Allsop, W., Bruce, T., Pearson, J., 2010. Breaking wave loads at vertical seawalls and breakwaters. Coastal Eng. 57 (4), 424–439. https://doi.org/10.1016/j.coastaleng.2009.11.005

Dimakopoulos, A.S., Guercio, A., Cuomo, G., 2014. Advanced numerical modelling of tsunami wave propagation, transformation and run-up. Proc. Inst. Civil Eng. - Eng. Comput. Mechan. 167 (3), 139–151. https://doi.org/10.1680/eacm.13.00029

Foster, A.S.J., Rossetto, T., Allsop, W., 2017. An experimentally validated approach for evaluating tsunami inundation forces on rectangular buildings. Coastal Eng. 128, 44–57. https://doi.org/10.1016/j.coastaleng.2017.07.006

Fujima, K., Achmad, F., Shigihara, Y., Mizutani, N., 2009. Estimation of tsunami force acting on rectangular structures. J. Disaster Res. 4, 404–409. https://doi.org/10.20965/jdr.2009.p0404

Fukui, N., Chida, Y., Zhang, Z., Yasuda, T., Ho, T.-C., Kennedy, A., Mori, N., 2021. Variations in building-resolving simulations of tsunami inundation in a coastal urban area. J. Waterway Port Coastal Ocean Eng. 148 (1). https://doi.org/10.1061/(ASCE)WW.1943-5460.0000690

Fukuyama, H., Kato, H., Ishihara, T., Tajiri, S., Tani, M., Okuda, Y., Kabeyasawa, T., Nakano, Y., 2012. Structural design requirement on the tsunami evacuation buildings. In: 14th U.S. - Japan Workshop on the Improvement of Structural Design and Construction Practices. Makena Alanui, Hawaii, USA.

Goring, D.G., 1978. Tsunamis - The Propagation of Long Waves onto a Shelf. Keck Lab Report Kh-R-38. California Institute of Technology. https://doi.org/10.7907/Z9MS3QPH

Goseberg, N., Wurpts, A., Schlurmann, T., 2013. Laboratory-scale generation of tsunami and long waves. Coastal Eng. 79, 57–74. https://doi.org/10.1016/j.coastaleng.2013.04.006

Goto, K., Ishizawa, T., Ebina, Y., Imamura, F., Sato, S., Udo, K., 2021. Ten years after the 2011 tohoku-oki earthquake and tsunami: geological and environmental effects and implications for disaster policy changes. Earth Sci. Rev. 212, 103417. https://doi.org/10.1016/j.earscirev.2020.103417

Graaf, J.W.v., Tromans, P., Vanderschuren, L., 1995. Wave loads on decks. Shell Offshore Struct. Eng. Newslett. 10, 15–18.

Hammack, J.L., Segur, H., 1974. The korteweg-de vries equation and water waves, II. comparison with experiments. J. Fluid Mech. 65, 289–313. https://doi.org/10.1017/S002211207400139X

Heller, V., Attili, T., Chen, F., Gabl, R., Wolters, G., 2021. Large-scale investigation into iceberg-tsunamis generated by various iceberg calving mechanisms. Coastal Eng. 163, 103745. https://doi.org/10.1016/j.coastaleng.2020.103745

Huo, C., Ma, L., Karmpadakis, I., 2025. The variability of wave-in-deck loading in random seas:a data-driven approach. Submitted to Applied Ocean Research. https://doi.org/10.2139/ssrn.5212988

Huo, C., Swan, C., Karmpadakis, I., Ma, L., et al., 2023. An efficient method of defining the tail of a crest height distribution. Ocean Eng. 289 (August), 116304. https://doi.org/10.1016/j.oceaneng.2023.116304

Inagaki, N., Nishida, Y., Mikami, T., Nakamura, R., Nistor, I., Soltanpour, M., Goseberg, N., Shibayama, T., 2025. Field survey of the 2024 noto peninsula earthquake and tsunami in japan: characteristics of damage patterns to coastal communities. Ocean Eng. 316, 119765. https://doi.org/10.1016/j.oceaneng.2024.119765

Jacobsen, N.G., Fuhrman, D.R., Fredsøe, J., 2012. A wave generation toolbox for the open-source CFD library: openfoam®. Int. J. Numer. Methods Fluids 70 (9), 1073–1088. https://doi.org/10.1002/fld.2726

Jiang, X., Yin, Z., Wang, Y., 2022. Numerical modelling of breaking wave interaction with the individual sections of a vertical cylinder using openFOAM®. Ocean Eng. 266, 112693. https://doi.org/10.1016/j.oceaneng.2022.112693

Karmpadakis, I., Swan, C., 2020. On the average shape of the largest waves in finite water depths. J. Phys. Oceanogr. 50 (4), 1023–1043. https://doi.org/10.1175/JPO-D-19-0165.1

Karmpadakis, I., Swan, C., 2022. A new crest height distribution for nonlinear and breaking waves in varying water depths. Ocean Eng. 266, 112972. https://doi.org/10.1016/j.oceaneng.2022.112972

Karmpadakis, I., Swan, C., Christou, M., 2019. Laboratory investigation of crest height statistics in intermediate water depths. Proc. Royal Soc. A 475 (2229), 20190183. https://doi.org/10.1098/rspa.2019.0183

Karmpadakis, I., Swan, C., Christou, M., 2020. Assessment of wave height distributions using an extensive field database. Coastal Eng. 157, 103630. https://doi.org/10.1016/j.coastaleng.2019.103630

Karmpadakis, I., Swan, C., Christou, M., 2022. A new wave height distribution for intermediate and shallow water depths. Coastal Eng. 175, 104130. https://doi.org/10.1016/j.coastaleng.2022.104130

Kasiman, E.H., 2017. Numerical Modelling of Wave Interactions with a Vertical Surface-piercing Column. Ph.D. thesis. Imperial College London. https://doi.org/10.25560/76335

Kistler, 2023. Press Force Sensor. Accessed 12 June 2025. https://www.kistler.cdn.celum.cloud/SAPCommerce_Download_original/002-475e.pdf.

Larsen, B.E., Fuhrman, D.R., 2019. Full-scale CFD simulation of tsunamis. part 1: model validation and run-up. Coastal Eng. 151, 22–41. https://doi.org/10.1016/j.coastaleng.2019.04.012

Lukkunaprasit, P., Ruangrassamee, A., Thanasisathit, N., 2009. Tsunami loading on buildings with openings. Science of Tsunami Hazards 28, 303–310.

Ma, L., Swan, C., 2020a. An experimental study of wave-in-deck loading and its dependence on the properties of the incident waves. J. Fluids Struct. 92. https://doi.org/10.1016/j.jfluidstructs.2019.102784

Ma, L., Swan, C., 2020b. The effective prediction of wave-in-deck loads. J. Fluids Struct. 95. https://doi.org/10.1016/j.jfluidstructs.2020.102987

Ma, L., Swan, C., 2023. An experimental study of wave-in-deck loading and its dependence on the properties of the topside structure. Mar. struct. 88, 103340. https://doi.org/10.1016/j.marstruc.2022.103340

Macabuag, J., Raby, A., Pomonis, A., Nistor, I., Wilkinson, S., Rossetto, T., 2018. Tsunami design procedures for engineered buildings: a critical review. Proc. Inst. Civil Eng. - Civil Eng. 171, 166–178.

Madsen, P.A., Fuhrman, D.R., Schaeffer, H.A., 2008. On the solitary wave paradigm for tsunamis. J. Geophys. Res. 113, C12012. https://doi.org/10.1029/2008JC004932

McGovern, D., 2016. Experiments on Tsunami Impact with a Vertical Sea Wall. 1st International Conference on Natural Hazards & Infrastructure; Conference date: 28-06-2016.

Miles, J.W., 1979. On the korteweg-de vries equation for a gradually varying channel. J. Fluids Mech. 91. https://doi.org/10.1017/S0022112079000100

Moris, J.P., Kennedy, A.B., Westerink, J.J., 2021. Tsunami wave run-up load reduction inside a building array. Coastal Eng. 169, 103910. https://doi.org/10.1016/j.coastaleng.2021.103910

Mulia, I.E., Heidarzadeh, M., Gusman, A.R., Satake, K., Fujii, Y., Sujatmiko, K.A., Meilano, I., Windupranata, W., 2024. Compounding impacts of the earthquake and submarine landslide on the toyama bay tsunami during the january 2024 noto peninsula event. Ocean Eng. 310, 118698. https://doi.org/10.1016/j.oceaneng.2024.118698

NCEI, 2024. Global historical tsunami database. Accessed 22 September 2024. https://www.ngdc.noaa.gov/hazel/view/hazards/tsunami/event-search.

Nouri, Y., Nistor, I., Palermo, D., Cornett, A., 2010. Experimental investigation of tsunami impact on free standing structures. Coastal Eng. J. 52 43–70. https://doi.org/10.1142/S0578563410002117

Palermo, D., Nistor, I., Al-Faesly, T., Cornett, A., 2012. Impact of tsunami forces on structures: the university of ottawa experience. In: Proceedings of the Fifth International Tsunami Symposium (ISPRA-2012). Tsunami Society International, Joint Research Centre, Ispra, Italy.

Park, H., Cox, D.T., Lynett, P.J., Wiebe, D.M., Shin, S., 2013. Tsunami inundation modelling in constructed environments: a physical and numerical comparison of free-surface elevation, velocity and momentum flux. Coastal Eng. 79, 9–21. https://doi.org/10.1016/j.coastaleng.2013.04.002

Park, H., Cox, D.T., Shin, S., 2019. Physical modeling of horizontal and vertical tsunami forces on the elevated overland structure. J. Coastal Res. 91 (SI), 51–55. https://doi.org/10.2112/SI91-011.1

Prasetyo, A., Tomiczek, T., Yasuda, T., Mori, N., Mase, H., Kennedy, A., 2013. Physical experiments of tsunami run-up and force on building cluster using a hybrid tsunami generator. Coastal Eng. 79, 9–21.

Rijnsdorp, D.P., Smit, P.B., Zijlema, M., 2014. Non-hydrostatic modelling of infragravity waves under laboratory conditions. Coastal Eng. 85, 30–42. https://doi.org/10.1016/j.coastaleng.2013.11.011

Rijnsdorp, D.P., Wolgamot, H., Zijlema, M., 2022. Non-hydrostatic modelling of the wave-induced response of moored floating structures in coastal waters. Coastal Eng. 177, 104195. https://doi.org/10.1016/j.coastaleng.2022.104195

Robertson, I.N., et al., 2024. Updates to Tsunami Design in ASCE 7-22. All Days. *International Ocean and Polar Engineering Conference*, pp. ISOPE–I–24–418.

Robertson, I.N., Chock, G., 2013. Performance of buildings and other structures during the tohoku tsunami. In: Research and Applications in Structural Engineering, Mechanics and Computation. Taylor and Francis Group, London, pp. 247–252.

Rossetto, T., Allsop, W., Charvet, I., Robinson, D.I., 2011. Physical modelling of tsunami using a new pneumatic wave generator. Coastal Eng. 58, 517–527. https://doi.org/10.1016/j.coastaleng.2011.01.012

Santo, J., Robertson, I.N., 2010. Lateral loading on vertical structural elements due to a tsunami bore. Technical Report UHM/CEE/10-02. University of Hawaii, College of Engineering, Department of Civil and Environmental Engineering.

Simamora, C., Shigihara, Y., Fujima, K., 2007. Experimental study on tsunami forces acting on structures. Proc. Coastal Eng. JCSE 54, 831–835. https://doi.org/10.2208/proce1989.54.831

Smit, P., Janssen, T., Holthuijsen, L., Smith, J., 2014. Non-hydrostatic modeling of surf zone wave dynamics. Coastal Eng. 83, 36–48. https://www.sciencedirect.com/science/article/pii/S037838391300149X. https://doi.org/10.1016/j.coastaleng.2013.09.005

Smit, P., Zijlema, M., Stelling, G., 2013. Depth-induced wave breaking in a non-hydrostatic, near-shore wave model. Coastal Eng. 76, 1–16. https://doi.org/10.1016/j.coastaleng.2013.01.008

St-Germain, P., Nistor, I., Townsend, R., Shibayama, T., 2014. Smoothed-particle hydrodynamics numerical modelling of structures impacted by tsunami bores. J. Waterway Port Coastal Ocean Eng. 140, 66–81. https://doi.org/10.1061/(ASCE)WW.1943-5460.00002

Suzuki, T., Altomare, C., Veale, W., Verwaest, T., Trouw, K., Troch, P., Zijlema, M., 2017. Efficient and robust wave overtopping estimation for impermeable coastal structures in shallow foreshores using SWASH. Coastal Eng. 122, 108–123. https://doi.org/10.1016/j.coastaleng.2017.01.009

Synolakis, C.E., 1987. On the runup of solitary waves. J. Fluid Mech. 185, 523–545. https://doi.org/10.1017/S002211208700329X

Synolakis, C.E., Bernard, E.N., 2006. Tsunami science before and beyond boxing day 2004. Philosophical Transactions of the Royal Society A 364 (1845), 2231–2265. https://doi.org/10.1098/rsta.2006.1824

Tadepalli, S., Synolakis, C.E., 1994. The run-up of n-waves on sloping beaches. Proc. Royal Soc. 445 (1923), 99–112. https://doi.org/10.1098/rspa.1994.0050

Thomas, S., Killian, J., Bridges, K., 2015. Influence of macrorougness on tsunami loading of coastal structures. J. Waterway Port Coastal Ocean Eng. 141 (1). https://doi.org/10.1061/(ASCE)WW.1943-5460.0000268

Thusyanthan, N.I., Madabhushi, S.P.G., 2008. Tsunami wave loading on coastal houses: a model approach. Civil Eng. 161, 77–86. https://doi.org/10.1680/cien.2008.161.2.77

Tomiczek, T., Prasetyo, A., Mori, N., Yasuda, T., Kennedy, A., 2016. Effects of a macro-roughness element on tsunami wave amplification, pressures, and loads: physical model and comparison to japanese and US design equations. Coastal Eng. J. 59 (1). https://doi.org/10.1142/S0578563417500048

Weller, H.G., Tabor, G., Jasak, H., Fureby, C., 1998. A tensorial approach to computational continuum mechanics using object-oriented techniques. Comput. Phys. 12 (6), 620–631. https://doi.org/10.1063/1.168744. https://doi.org/10.1063/1.168744

Winter, A.O., Alam, M.S., Shekhar, K., Motley, M.R., Eberhard, M.O., Barbosa, A.R., Lomonaco, P., Arduino, P., Cox, D.T., 2020. Tsunami-like wave forces on an elevated coastal structure: effects of flow shielding and channelling. J. Waterway Port Coastal Ocean Eng. 146 (4). https://doi.org/10.1061/(ASCE)WW.1943-5460.000058

Yeh, H., 2007. Design tsunami forces for onshore structures. Journal of Disaster Research 2 (6), 531–536. https://doi.org/10.20965/jdr.2007.p0531

Zhang, Z., Kennedy, A.B., Moris, J.P., 2023. Tsunami wave loading on a structural array behind a partial wall. Coastal Eng. 179, 104244. https://doi.org/10.1016/j.coastaleng.2022.104244

Zijlema, M., Stelling, G., Smit, P., 2011. Swash: an operational public domain code for simulating wave fields and rapidly varied flows in coastal waters. Coastal Eng. 58 (10), 992–1012. https://doi.org/10.1016/j.coastaleng.2011.05.015